



## ISTITUTO NAZIONALE DI RICERCA METROLOGICA Repository Istituzionale

Characterisation and modelling of water wicking and evaporation in capillary porous media for passive and energy-efficient applications

This is the author's submitted version of the contribution published as:

*Original*

Characterisation and modelling of water wicking and evaporation in capillary porous media for passive and energy-efficient applications / Alberghini, Matteo; Boriskina, Svetlana V.; Asinari, Pietro; Fasano, Matteo. - In: APPLIED THERMAL ENGINEERING. - ISSN 1359-4311. - 208:(2022), p. 118159. [10.1016/j.applthermaleng.2022.118159]

*Availability:*

This version is available at: 11696/75379 since: 2023-02-02T15:32:25Z

*Publisher:*

PERGAMON-ELSEVIER SCIENCE LTD

*Published*

DOI:10.1016/j.applthermaleng.2022.118159

*Terms of use:*

This article is made available under terms and conditions as specified in the corresponding bibliographic description in the repository

*Publisher copyright*

(Article begins on next page)

# Characterisation and modelling of water wicking and evaporation in capillary porous media for passive and energy-efficient applications

Matteo Alberghini<sup>a,b,c</sup>, Svetlana V. Boriskina<sup>a</sup>, Pietro Asinari<sup>b,d</sup>, Matteo Fasano<sup>b,c,\*</sup>

<sup>a</sup>*Massachusetts Institute of Technology, 77 Mass. Ave., Cambridge, MA*

<sup>b</sup>*Politecnico di Torino, Department of Energy, Corso Duca degli Abruzzi 24, Torino*

<sup>c</sup>*Clean Water Center, Corso Duca degli Abruzzi 24, Torino*

<sup>d</sup>*Istituto Nazionale di Ricerca Metrologica, Strada delle Cacce 91, Torino*

---

## Abstract

Passive devices based on water wicking and evaporation offer a robust, cheap, off-grid, energy-efficient and sustainable alternative to a wide variety of applications, ranging from personal thermal management to water treatment, from filtration to sustainable cooling technologies. Among the available, highly-engineered materials currently employed for these purposes, polyethylene-based fabrics offer a promising alternative thanks to the precise control of their fabrication parameters, their light-weight, thermal and mechanical properties, chemical stability and sustainability. As such, both woven and non-woven fabrics are commonly used in capillary-fed devices, and their wicking properties have been extensively modelled relying on analytical equations. However, a comprehensive and flexible modelling framework able to investigate and couple all the heat and mass transfer phenomena regulating the water dynamics in complex 2-D and 3-D porous components is currently missing. This work presents a comprehensive theoretical model aimed to investigate the wetting and drying performances of hydrophilic porous materials depending on their structural properties and on the external environmental conditions. The model is first validated against experiments, then employed in three application cases: the characterisation of the capillary properties of a novel textile; the assessment of the thermal performance of a known material for personal thermal management when used in different conditions; the model-assisted design of a porous hydrophilic component of passive devices for water desalination. The obtained results showed a deep interconnection between the different heat and mass transfer mechanisms, the porous structure and external working conditions. Thus, modelling their non-linear behaviour plays a crucial role in determining the optimal material characteristics to maximise the performance of porous materials for passive devices for the energy and water sector.

**Keywords:** Energy efficiency, Water-Energy nexus, Passive devices, Porous media, Multiphysics modelling

---

---

\*Corresponding Author

<b>Nomenclature</b>			$I$	Current	A
<b>Greek letters</b>			$I_{rr}$	Specific incident irradiance	W/m <sup>2</sup>
$\alpha$	Optical absorption coefficient	-	$K$	Absolute permeability	m <sup>2</sup>
$\beta$	Van Genuchten's parameter	1/m	$k$	Thermal conductivity	W/(m·K)
$\epsilon$	Optical emissivity coefficient	-	$k_r$	Relative permeability	-
$\lambda$	Wavelength	m	$k_u$	Coverage factor for uncertainty evaluation	-
$\mu$	Viscosity	Pa·s	$L$	Van Genuchten's parameter	-
$\omega$	Width of the transition zone of the ramp function	-	$M_w$	Molecular weight of water	kg/mol
$\phi$	Porosity	-	$n$	Van Genuchten's parameter	-
$\rho$	Density	kg/m <sup>3</sup>	$p$	Pressure	Pa
$\tau$	Optical transmission coefficient	-	$p_c$	Capillary pressure	Pa
$\Theta$	Normalised saturation content	-	$P_{in}$	Input power	W
$\theta$	Solid angle	sr	$p_{sat}$	Saturation pressure	Pa
<b>Symbols</b>			$q_b$	Boundary heat losses through the bottom side of the setup	W/m <sup>2</sup>
$\Delta T$	Temperature Difference	°C	$q_c$	Convective boundary heat flux	W/m <sup>2</sup>
$\dot{m}_{ev}$	Theoretical specific evaporation rate	kg/(m <sup>2</sup> s)	$Q_e$	Evaporative volumetric heat flux	W/m <sup>3</sup>
$\hat{\mathbf{n}}$	Versor perpendicular to a boundary surface	J/(kg·K)	$q_r$	Radiative boundary heat flux	W/m <sup>2</sup>
$\mathbf{g}$	Gravitational acceleration	m/s <sup>2</sup>	$q_{in}$	General input specific heat flux	W/m <sup>2</sup>
$\mathbf{v}$	Fluid velocity	m/s	$R$	Sample radius	m
$\mathbf{v}_D$	Darcy's velocity coefficient	m/s	$r$	Optical reflection coefficient	-
$A_s$	Sample surface	m <sup>2</sup>	$R_g$	Universal gas constant	J/(kg·mol)
$C$	Dimensional fitting constant	m/s <sup>-1/2</sup>	$RH$	Relative humidity	-
$c$	General fitting or integration constant	-	$S$	Pores saturation content	-
$c_p$	Specific heat at constant pressure	J/(kg·K)	$S_r$	Residual saturation content	-
$d_z$	Textile thickness	m	$T$	Temperature	°C
$E$	Evaporation rate constant	-	$t$	Time	s
$E_r$	Black-body emissivity	W/(m <sup>3</sup> sr)	$T_{sky}$	Sky temperature	K
$f$	Mass source/sink term	kg/(m <sup>3</sup> s)	$V$	Electric potential	V
$g_a$	Air gap thickness	m	$V_w$	Volume of wicked water	m <sup>3</sup>
$h$	Convection coefficient	W/(m <sup>2</sup> K)	$w$	Width of a sample	m
$h_m$	Maximum height reached in vertical imbibition	m	$x, y$	Reference coordinates	m
$h_t$	Front height evaluated at the time $t$	m	Ra	Rayleigh number	-
$H_{ev}$	Enthalpy of vaporisation	J/kg	<b>Subscripts and superscripts</b>		
$h_{out}$	Convection coefficient in outdoor conditions	W/(m <sup>2</sup> K)	0	Initial value	

$a$	Ambient
$dry$	Dry fabric property
$eff$	Porosity-averaged effective property
$ext$	External radiative source ( <i>i.e.</i> solar light)
$F$	Fluid domain property
$f$	Fabric property
$f \rightarrow a$	Fabric to ambient
$h$	Silicone heater property, the substrate of the fabric
$int$	Internal radiative source, <i>i.e.</i> the fabric or the heater surfaces
$m$	Porous matrix property
$nw$	Non-wetting fluid
$p$	Reference coordinates in pixels
$v$	Water vapour property
$w$	Wetting fluid
$wet$	Wet fabric property

## 1. Introduction

Water wicking and evaporation are crucial phenomena in a broad variety of industrial applications, including food processing, filters, soil science, composite materials, heat pipes and oil recovery [1–3]. Recently, the interest in water wicking and evaporation from porous materials has exponentially increased due to the study of passive technologies for addressing the water-energy nexus, most of which rely on hydrophilic porous media. Such devices do not require high-quality energy inputs and, thanks to the absence of mechanical moving parts, need low maintenance, are cheap and usually made by off-the-shelves materials. Furthermore, they are optimal for off-grid installations and, in general, promote the sustainable transition towards the water-energy nexus. As the performance of these passive systems are strictly determined by the efficiency of the heat and mass transfer mechanisms involved, their comprehension is crucial to correctly design novel porous materials with optimised performance. In particular, applications of such passive technologies may involve both woven or non-woven textiles, and range from personal thermal management [4–6] to water desalination [7–11], from solar steam generation [12, 13] to atmospheric water extraction [14, 15], from filtration [16] to cooling technologies [17–19].

In this context, polymer-based fabrics offer a promising alternative to traditional materials (e.g. cotton, linen and silk) thanks to their outstanding structural [20], thermal [21], mechanical [22] and optical [23] performance, and to their sustainability [24]. For example, polyethylene (PE) fibers presents 4.5 and 2.5 times lower environmental impact with respect to cotton and nylon, respectively [25], and can be easily recycled [26]. Current fabrication techniques allow a great control on a wide range of fabrication parameters and physical properties, both at the nano/microscopic level (e.g. the fibers geometry and size [27], surface chemistry and functionalisation [4], thermal conductivity [21]) and at the macroscopic one (*i.e.* non-woven structure, knitted or woven patterns, mechanical resistance).

The capillary properties of porous media (including polymer-based fibrous fabrics) are determined by their micro-scale structure and surface chemistry. A common modelling approximation requires to compare the properties of the porous matrix to a bundle of parallel tubes, retrieving a simplified analytical model describing the dynamic wicking [28–30] that, however, only allows to investigate 1-dimensional (1-D) processes [1]. As several recent studies proposed passive devices with 2-D or 3-D geometries exploiting capillary suction [9, 31–35], the modelling framework should shift to a continuum description, enabling a finite element implementation of the mass transfer phenomena suitable to investigate the combined effects of more complex topologies. Furthermore, this approach becomes crucial when water transport and evaporation are affected by non-negligible heat fluxes due to conduction, convection and radiative heat transfer, e.g. in solar distillation

and personal thermal management applications.

In this work we develop a comprehensive model for the heat and mass transfer phenomena in hydrophilic media characterised by a 3D distribution of pores. In particular, sections 2 and 3 will cover the procedure used to characterise a novel woven PE fabric, specifically designed for personal thermal management. The heat and mass transfer mechanisms involved are inherently coupled, thus the problem is divided into three sub-problems, which were individually experimentally investigated and theoretically formulated according to the schematic Supplementary Fig. S1: wicking (blue box), evaporative (green box) and radiative heat transfer (red box). The characterised material-dependent parameters and the validated comprehensive model can be eventually used to perform sensitivity analyses or simulate particular case-studies. The detailed characterisation procedure is reported in Supplementary Figs. S2 and S3: a computerised micro tomography (micro-CT, purple boxes), was used to evaluate the average yarn porosity, thickness and surface roughness of the woven PE fabric, which are input parameters common to all the transfer mechanisms analysed. The methodology used for the characterisation of the capillary properties was both experimental and numerical (see Supplementary Fig. S2A, blue boxes): horizontal imbibition tests were used to evaluate the absolute permeability of the fabric, while vertical imbibition tests to fit the material-dependent Mualem-van Genuchten’s parameters by a simplified 1-dimensional finite elements model. The evaporative cooling performances of the woven PE fabric were evaluated by a wet-to-dry experimental cycle; then, the coupled heat and mass transfer model was used to evaluate the evaporation rate by comparing the experimental and numerical results (see Supplementary Fig. S2B, green boxes). Finally, a similar experimental procedure was used to assess its radiative performances (see Supplementary Fig. S3): the optical properties of the fabric and of its substrate were evaluated by a spectrometric analysis (purple boxes); then, the model was validated by comparing the temperature transients obtained from indoor and outdoor experiments with the results of steady-state simulations. The described methodology also required a few complementary simulations to characterise the experimental setup (see the dash-dotted boxes in Supplementary Figs. S2 and S3). The outcomes of the material characterisation and of the model validation were employed to implement two case-studies: assessing how different environmental conditions affect the thermal performance of the woven PE textile in the context of passive thermal management applications (see section 4.1); evaluating the combined effects of the capillary and geometrical properties on the design constraints of a component for passive and energy-efficient desalination devices, given a specific working condition (see section 4.2).

Despite the focus is set on polyethylene-based fibrous textiles to allow model validation, the theoretical framework developed does not lose its generality and allows a

more rational characterisation and design of porous materials in several fields. For illustrative purposes, three different applications are envisioned for the proposed comprehensive model in the broad field of water-energy nexus: (i) to characterise material-dependent properties of novel porous materials, if supported by a minimal experimental investigation; (ii) to investigate the thermal performance of a known porous material in a wide range of working conditions; (iii) to design the optimal physical properties and geometrical features of novel porous components for passive devices, compliant to application-specific constraints.

## 2. Experimental investigation

### 2.1. Fabrication and characterisation of the textile

#### 2.1.1. Methods

The representative woven PE textile was composed of micro-fibers created by the standard melt spinning process, using a blend of linear low-density polyethylene (LLDPE) and high-density polyethylene (HDPE) granules and pellets (Alpha Aesar). The yarns were composed of 247 fibers each and were woven into plain-weave textile through an industrial scale loom at the Shingora Textile ltd.

To measure the average porosity  $\phi$  of the yarn and the average thickness  $d_z$  of the plain-woven PE textile, a high-resolution micro-computed tomography (micro-CT) scanner (Zeiss Xradia 620 Versa) was employed (see Fig. 1A). The obtained images were post-processed to measure the ratio between the white (void) and black (fibers) pixels within the yarn, thus estimating the textile porosity. Further details on the manufacturing process and the procedure used for characterising the micro-structure of the textile is reported in Ref. [4].

The heat transfer between a fabric and its supporting substrate is affected by the average thickness of the air gap between the two surfaces, which hinders their thermal contact. The air gap  $g_a$  was estimated by a MATLAB® image processing routine applied on the sections obtained via the micro-CT, where the textile sample was horizontally placed (at rest) on a smooth stage within the equipment.  $g_a$  was evaluated as the average distance between the first layers of fibers and the supporting plane (see Fig. 1B). Thus, 23 images, each containing the cross section of 5 yarns, had a resolution of  $2.732 \cdot 10^{-6}$  m/px and were converted to binary images and analysed. The surface roughness observable from the micro-CT images (see Fig. 1A, section S-S) was used to evaluate the average distance between the sample surface and a given rigid support plane (see Fig. 1B, blue curve). As it can be observed in Fig. 1B, the images were not planar, thus the profile was fitted with a first grade polynomial  $y'_p = c_1 x_p + c_2$ , where  $x_p$  is the horizontal position of the textile boundary in px. The average distance of the textile from the plane  $g_a$ , expressed in meters, was evaluated as twice the average distance of

each point of the profile from the fitting line:

$$g_a = 2.732 \cdot 10^{-6} \cdot \frac{2(y_p - y'_p)}{\sqrt{1 + c_1^2}}, \quad (1)$$

where  $y_p$  is the measured position of the textile boundary at a given  $x_p$ . The procedure was repeated for the upper profile (see Fig. 1B, solid red line) and the results averaged.

#### 2.1.2. Results

The fibers within the yarns were closely packed and moderately parallel. Hence, the micro-structural parameters of the woven PE were evaluated as  $\phi = (53.0 \pm 4.8) \%$ ,  $d_z = (346 \pm 51) \mu\text{m}$  and radius  $(18.5 \pm 6.2) \mu\text{m}$ . The micro-CT images were also used to evaluate the air gap between the fabric and an horizontal supporting surface resulting in  $g_a = (7.1 \pm 3.4) \cdot 10^{-5}$  m. The reported expanded uncertainty was evaluated as the standard deviation of the 46 measurements considered, with a coverage factor  $k_u = 2$  [36].

### 2.2. Wicking

#### 2.2.1. Methods

The wicking performance of the woven textile were investigated by horizontal and vertical wicking tests. The analysed samples were approximately 20 cm high and 2.5 cm wide. The bottom end of the fabric samples were dipped approximately 2 mm deep into a box filled with distilled water. An infrared camera (FLIR ETS230) was used to measure the time-dependent position of the water front  $h_t$  for 45 seconds, in case of horizontal imbibition, and for 10 minutes, in case of vertical tests. The experiments were performed at controlled ambient conditions. The obtained images were post-processed via the MATLAB® Image Processing toolbox. A schematic of the characterisation procedure is represented in Fig. 2A-C. The setup was also used to measure the maximum height  $h_m = h_t|_{t \rightarrow \infty}$  reached by the water front in a vertical wicking test. An extensive description of the experimental procedure employed to measure the vertical wicking performance and  $h_m$  is reported in Ref. [4].

To assess the horizontal wicking performance, the sample was placed on a polytetrafluoroethylene (PTFE) surface and dipped approximately 1 mm deep into the distilled water reservoir. The PTFE surface was chosen for its hydrophobicity, thus avoiding to interfere with the dynamic imbibition process. The absolute permeability  $K$  of the plain woven PE was evaluated from the time-dependent position of the water front  $h_t$  obtained from the horizontal wicking test. As the effect of gravity can be neglected,  $h_t$  can be computed as [1]:

$$h_t = \sqrt{\frac{2Kp_c}{\phi\mu_w}t}, \quad (2)$$

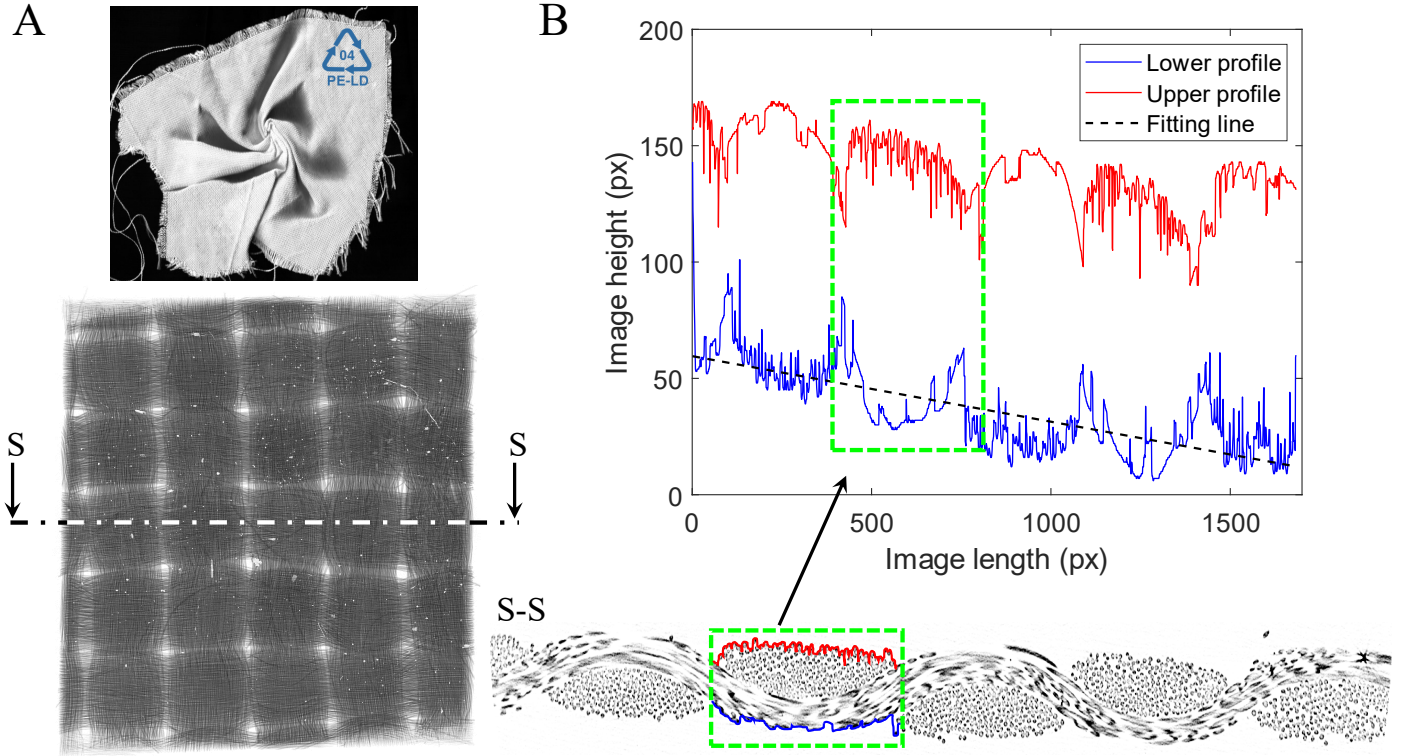


Figure 1: **Characterisation of the textile micro-structure.** (A) Image of the polyethylene textile (reproduced from Ref. [4]) and its 3-dimensional reconstruction from Micro-CT, obtained from the digital assembly of 541 sections (S-S). (B) The images of 23 different sections were post processed to evaluate the average thickness of the air gap  $g_a$  between the horizontal fabrics (considered at rest) and its support. The processed images were used to evaluate the lower (blue line) and upper (red line) boundary of the fabric.  $g_a$  was evaluated as twice the average distance of the lower profile from its fitting line (dashed black line).

where  $p_c$  is the capillary pressure,  $\phi$  the fabric porosity and  $\mu_w$  is the dynamic viscosity of the wetting fluid. Considering the textile as an isotropic and rigid porous medium, Eq. 2 can be written in the form:  $h_t = C\sqrt{t}$ , where  $C$  is a constant which can be evaluated from the experimental observations of  $h_t$  by least squares fitting. Thus, the absolute permeability  $K$  results to be:

$$K = \frac{C^2 \phi \mu_w}{2p_c}. \quad (3)$$

### 2.2.2. Results

The maximum height  $h_m$  reached by the water front in the vertical imbibition test is directly related to the capillary pressure  $p_c$ , which is the macro-scale counterpart of the micro-scale structure, namely the arrangement of the fibers in the yarn [37, 38]. At the equilibrium,  $p_c$  balances the height of the water column wicked within the porous medium, thus the capillary pressure can be evaluated as  $p_c = \rho_w |\mathbf{g}| h_m$ , being  $\rho_w$  the density of the wetting fluid and  $\mathbf{g}$  the gravitational acceleration. Averaging the results of three repetitions, the maximum height was evaluated as  $h_m = (13.8 \pm 0.8)$  cm. Further details on the evaluation of the uncertainty are reported in Supplementary Note 1.

Fig. 2D reports the results of the vertical (main figure) and horizontal (inset) wicking experiments. The time

dependent position of the water front  $h_t$  can be described under the sharp front approximation [1] (see Fig. 2A-C), thus Eq. 2 can be used to fit the data (inset of Fig. 2D, black dashed line). The data obtained from the horizontal setup were used to evaluate the absolute permeability of the textile  $K$  to water from Eq. 3, which was evaluated as  $K = (7.1 \pm 1.8) \cdot 10^{-12} \text{ m}^2$ . Notice that water evaporation had a negligible effect on the measured values of  $h_m$  during the wicking test (see Supplementary Note 2 for further details).

### 2.3. Evaporation

#### 2.3.1. Methods

The setup and experimental protocol used to investigate the effect of evaporative cooling on the textile temperature is schematised in Fig. 3A. The setup was composed of a polystyrene parallelepiped (2 cm thick, 10 cm x 10 cm wide), a thermistor (model 4033, Omega instruments) placed at the center of the specimen and three other thermistors placed in the radial direction with an equal spacing of 1 cm, which were used to measure its surface temperature. First,  $(0.25 \pm 0.02)$  ml of distilled water were placed at the center of the setup (see Fig. 3A, step 1). Then, a fabric sample (radius  $R = 5$  cm) was manually placed on the setup, the water droplet was absorbed and spread



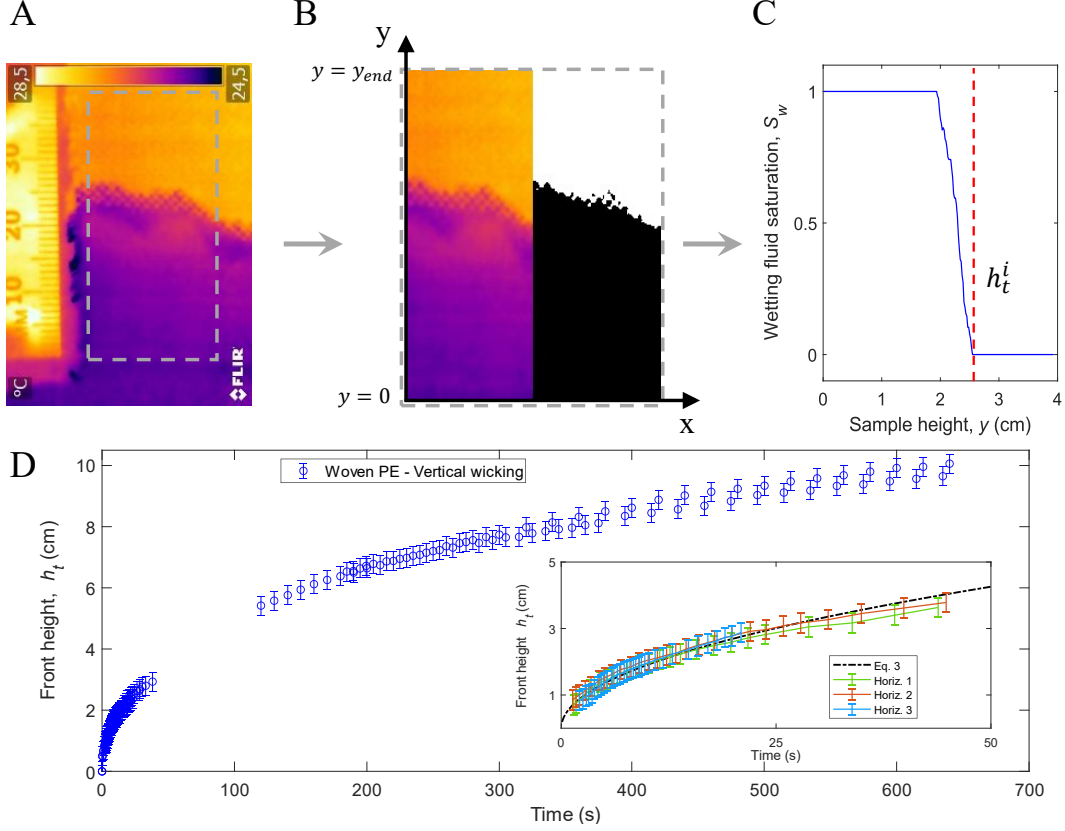


Figure 2: **Experimental investigation of the wicking performance.** (A) A frame extracted from the video recorded with the IR camera during the vertical wicking of the PE fabric by water. The aluminium ruler is used to estimate the conversion scale from px to mm. The difference between the optical properties of the wet (purple) and dry (orange) zones of the textile allows their simple distinction. (B) The central part of the textile sample was converted to binary black/white image and used to estimate the position and thickness of the water front. The homogeneity of the front allows to reduce the complexity of the system from 2-D to 1-D. (C) The saturation was averaged along the width of the sample to obtain an equivalent 1-dimensional saturation curve along the  $y$  axis. The height of the water front during the  $i$ -th measurement  $h_t^i$  was evaluated as the first point satisfying the constraint  $S_w \leq 0.05$ . (D) Results of the vertical (main plot) and horizontal (inset) wicking tests. The former were originally presented in Ref. [4]. The data obtained from the horizontal test, the porosity  $\phi$  and the capillary pressure  $p_c$  are used to retrieve the permeability through Eq. 3. The detailed procedure to evaluate the reported uncertainties is described in Supplementary Note 1.

within the textile by capillary action, and allowed to dry at room temperature  $T_a = (23.9 \pm 0.4)^\circ\text{C}$  with a controlled relative humidity of  $RH = (0.40 \pm 0.05)$  (see Fig. 3A, step 2). The ambient temperature was measured with a thermistor (model 4033, Omega instruments), while the relative humidity with an hygrometer (RH820, Omega instruments). The temperatures measured by the thermistors were sampled with a frequency of 1 Hz until complete evaporation.

### 2.3.2. Results

The results of the drying experiment are reported in Fig. 3B. The homogeneity of the measured temperature distribution is due to the efficient spreading of the water droplet, which was rapidly wicked within the textile as soon as it was deposited at  $t = 0$ , and to the uniform evaporation rate over the sample surface. Notice that, the examined textile is composed by non-porous fibers, which, in contrast with natural fibers, do not absorb water within their volume. As a consequence, the temperature

measured by all the thermistors at the end of the drying transient quickly recovers its initial value (see Fig. 3B, from 30 min to 40 min). This experiment is used to evaluate the dimensionless evaporation rate constant  $E$ , which strongly depends on the environmental conditions (see section 3.2.1) and is essential to correctly model evaporation.

## 2.4. Radiation

### 2.4.1. Methods

The effect of the optical properties of the textile on its radiative heat transfer was experimentally investigated both indoor and outdoor. A schematic of the experimental setup is represented in Fig. 4A. Two silicone heaters (SRFRA-4/5-P, Omega instruments) were used to provide a constant heat flux to the fabric during the experiments. Two thermistors (model 4033, Omega instruments) were applied with a high thermal conductivity paste at the center and at 1 cm from the boundary of the top surface of each heater. A digital data logger (OM-CP-OCTPRO, Omega instruments) was used to measure the temperature



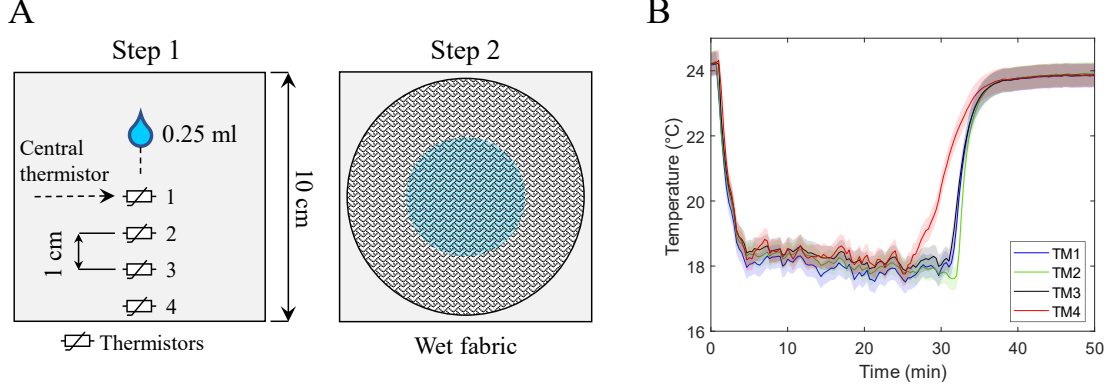


Figure 3: **Experimental investigation of water evaporation performance.** (A) Schematic of the experimental setup for assessing the evaporation of wetting fluid from the textile. *Step 1*: four thermistors were used to evaluate the temperature distribution during the test. A  $(0.25 \pm 0.2)$  ml droplet was poured with a micro-syringe on the central thermistor. *Step 2*: the dry fabric sample was placed on the setup, the water droplet was absorbed and spread within the textile, and evaporation started. The effect of evaporative cooling on the substrate temperature, assumed to be approximately equal to the textile temperature, was assessed by four thermistors. (B) Radial temperature distribution in a circular woven PE textile during the evaporation test described in section 3.2.1. The numbered temperature curves respectively refer to the thermistors shown in panel A. The solid lines represent the average values and their shaded contour their uncertainty. The detailed procedure to evaluate the reported uncertainties is described in Supplementary Note 1.

of the thermistors with a sampling frequency of 1 Hz. The lower surface of the heater was attached to two identical polystyrene boxes (8 cm thickness, 20 cm x 13 cm width) to minimise the heat losses downwards. The heaters were connected in parallel to a power supplier, which provided a current of  $I = 0.143$  A and a voltage of  $V = 15.7$  V to the circuit. Thus, each heater was constantly supplied with  $P_{in} = 1.12$  W for the duration of the experimental campaign. During outdoor experiments, a pyranometer (LP PYRA 08, Delta Ohm) was used to measure the incoming solar radiation. At the beginning of indoor tests, the power supplied was switched on and the two heaters were left uncovered until the steady state was reached (*i.e.* when the temperature readings were statistically comparable). Afterwards, a dry circular textile sample ( $R = 5$  cm) was placed above one silicone heater. The steady state was considered reached when the standard deviation of at least 1000 temperature acquisitions was lower than  $0.1$  °C. Then, the equilibrium temperature was measured for approximately 4000 s and the average value and its standard deviation evaluated.

The optical transmittance and reflectance of the fabric and the reflectance of the painted surface of the heater in the ultraviolet (UV), visible (VIS) and near-infrared (NIR) ranges were evaluated via a UV-VIS spectrometer (Agilent Cary 5000) equipped with an integrating sphere. The infrared (IR) transmittance and reflectance of the fabric were evaluated with an infrared-diffuse-gold-coated integrating sphere (PIKE technologies) with an FTIR spectrometer (Thermo Nicolet 5700). The optical coefficients were obtained by averaging three measurements, each referenced to a blank test.

#### 2.4.2. Results

The experimental setup described in section 2.4.1 and Fig. 4A was used to evaluate the radiative heat transfer properties of the textile by measuring the temperature difference between the covered and uncovered setups, both indoor and outdoor. Note that the two setups used are identical. The results of indoor test are shown in Fig. 4B. The temperature difference between the central (blue and green solid lines) and the boundary (red and magenta solid lines) thermistors before placing the fabric on one of the setups (dashed black line) was negligible. Then, after a transient of approximately 25 minutes, the steady state was reached, and the temperature difference between the covered and the uncovered setup was  $\Delta T = (3.5 \pm 0.5)$  °C or  $\Delta T = (2.9 \pm 0.5)$  °C, considering respectively the central or the boundary. However, the surface temperature of the heaters was not homogeneous: the measured temperature difference between the two thermistors placed at the center and on the boundary of the heaters were  $\Delta T_{cov} = (2.3 \pm 0.5)$  °C and  $\Delta T_{unc} = (2.9 \pm 0.5)$  °C, respectively for the covered and uncovered setups. The discrepancy between the two values is coherent with their uncertainty and, therefore, statistically comparable. Thus, the measured surface temperature of the uncovered setup was used to evaluate the non-homogeneous heating characteristic proper of the silicone heaters, modelled as a linear function of the heater radius  $R$ , and the optical absorption coefficient of the white paint  $\bar{\alpha}_h$  following the numerical procedure described in Supplementary Note 3. An iterative least-squares fitting was used to minimise the discrepancy between the average measured temperatures and those computed from a steady-state finite elements simulation, which led to  $\bar{\alpha}_h = 0.866$  and  $c_5 = -c_6 = 0.169$  (see Supplementary Note 3 for further details).

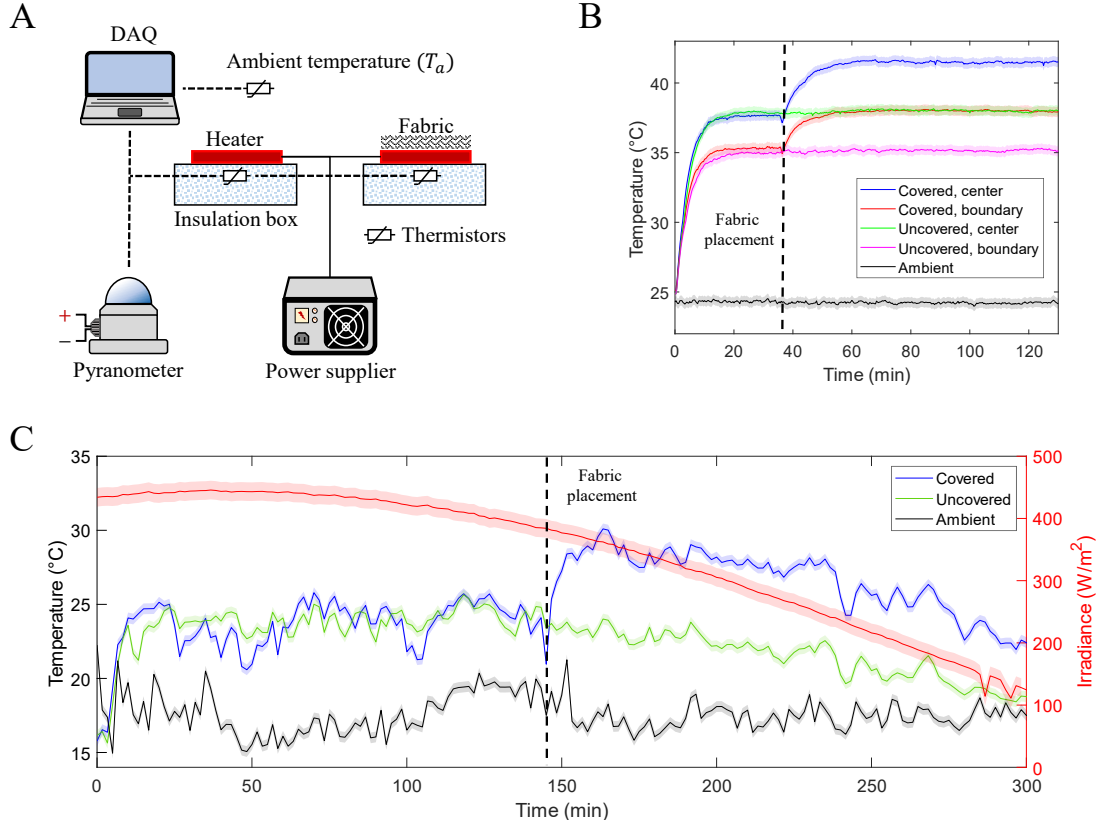


Figure 4: **Experimental investigation of the radiative heat transfer performances.** (A) Schematic of the experimental setup to assess the thermal performances of the fabric either indoor or outdoor. Two heaters were connected in parallel to a power supplier. The surface temperature of the two heaters was monitored with two thermistors each, while the solar radiation and the ambient temperature were measured with a pyranometer and a thermistor, respectively. (B) Results of the indoor test. The temperature difference measured by the thermistors at the center (solid blue and green curves) and at the boundary (solid red and magenta curves) of the heaters is due to the non-homogeneous distribution of the input heat. The solid lines represent the average values and their shaded contour their uncertainty (see Supplementary Note 1), which is the same for both configurations. (C) Results of the outdoor test. The plot reports only the temperatures measured by the thermistor placed at the center of the specimens. The solid lines represent the average values and their shaded contour their uncertainty (see Supplementary Note 1).

The results of outdoor test are presented in Fig. 4C, where only the temperature transients of the central thermistors were reported. The test was performed supplying  $P_{in} = 1.12 \text{ W}$ , as during the indoor test, while the noise affecting the temperature readings is due to the wind. First, the two setups were both left uncovered for approximately 150 mins. At this stage, the average temperature difference between the two heaters was negligible. As soon as one of the heaters was covered (approximately at minute 150, solid blue line), the measured temperature increased. The effect of the sun is blatant: as the solar radiation progressively decreased from  $450 \text{ W}/\text{m}^2$  to  $100 \text{ W}/\text{m}^2$ , so did  $\Delta T$ , ranging from approximately  $6.5^{\circ}\text{C}$  to approximately  $4^{\circ}\text{C}$ , both higher with respect to the indoor setup. This result highlights the importance of tailoring the UV-VIS-NIR properties to achieve the desired outdoor performance (e.g. heating or cooling).

Due to the presence of variable wind speed, the convection coefficient  $h$  was evaluated by an iterative least-squares fitting procedure, which aimed to minimise the difference between temperatures computed in a represen-

tative setup – modelled by a finite elements model – and the average experimental temperature of the uncovered setup. The simulations were performed considering as target temperature  $T_h = 23.9^{\circ}\text{C}$ , relative humidity  $RH = 0.4$ , ambient temperature  $T_a = 17.5^{\circ}\text{C}$  and solar irradiance  $I_{rr} = 426 \text{ W}/\text{m}^2$ , which were obtained averaging the respective experimental values in the first 100 mins of experiment. The resulting equivalent convection coefficient representative of the tested outdoor conditions was evaluated as  $h_{out} = 22.2 \text{ W}/(\text{m}^2\text{K})$ .

### 3. Theoretical model

#### 3.1. Wicking

##### 3.1.1. Methods

The dynamic imbibition of a single-phase fluid (water) in a rigid porous material (yarn) under isothermal condi-

tion was modelled by combining the Darcy's law:

$$\mathbf{v}_D = -\frac{Kk_{r,w}}{\mu}(\nabla p_w + \rho_w \mathbf{g}), \quad (4)$$

and the mass conservation of the wetting fluid [39]:

$$\frac{\partial \rho}{\partial t} + \nabla \cdot (\rho \mathbf{v}) = -f, \quad (5)$$

where  $\mathbf{v}_D$  the Darcy's velocity,  $p_w$  is the pressure field of the wetting fluid,  $k_{r,w}$  the relative permeability for the wetting fluid. Furthermore,  $\rho$  is the density of the liquid phase within the porous medium,  $\mathbf{v}$  is the velocity field, and  $-f$  is the sink term representing the evaporation rate of the wetting fluid. Eqs. 4 and 5 can be combined considering that:

$$\begin{aligned} \rho &= \rho_w S_w \phi, \\ \mathbf{v} &= \frac{\mathbf{v}_D}{S_w \phi}, \end{aligned} \quad (6)$$

where  $S_w$  is defined as the saturation of the wetting fluid.  $S_w$  is defined as the ratio between the volume occupied by the wetting fluid and the total volume of the pores, thus it ranges from 0 to 1. Considering the saturation of the wetting fluid  $S_w$  (*i.e.* water) and of the non-wetting fluid  $S_{nw}$  (*i.e.* air), it holds:

$$S_w + S_{nw} = 1. \quad (7)$$

$S_w$  is generally normalised considering its irreducible fraction  $S_{r,w}$ , namely the minimum amount of wetting fluid always present in the porous matrix, and the residual fraction of the non-wetting fluid  $S_{r,nw}$  [40, 41]:

$$\Theta_w = \frac{S_w - S_{r,w}}{1 - S_{r,nw} - S_{r,w}}, \quad (8)$$

which bounds the saturation of the wetting fluids in the range  $S_{r,w} \leq S_w \leq 1 - S_{r,nw}$ . However, given the arrangement of the fibers composing the yarn and the tightly-woven structure of the fabric, in the present work it was assumed  $S_{r,nw} = 0$  and  $S_{r,w} = 0$ . These assumptions led to  $\Theta_w = S_w$ , meaning that the porous structure is totally connected and accessible to water, and that the water can completely evaporate from the fabric.

In the limit of incompressible fluid and of a rigid porous matrix, Eqs. 4, 5 and 6 can be combined as:

$$\rho_w \phi \frac{\partial S_w}{\partial t} + \nabla \cdot \left[ -\rho_w \frac{Kk_{r,w}}{\mu} (\nabla p_w + \rho_w \mathbf{g}) \right] = -f. \quad (9)$$

Eq. 9 can be solved if a relationship between  $p_w$  and  $S_w$  is provided. For this purpose, the capillary pressure and a retention model needs to be introduced. The capillary pressure  $p_c$  is defined as the difference between the pressure of the non-wetting and wetting fluids at their interface,

namely:

$$p_c = p_{nw} - p_w. \quad (10)$$

A retention model, instead, explicitly formalizes the dependency of the capillary pressure with the saturation of the pores, thus  $\Theta_w = \Theta_w(p_c)$ . One of the most widely used retention functions was proposed by van Genuchten [42]:

$$\Theta_w = \left( \frac{1}{1 + \left| \beta \frac{p_c}{\rho_w g} \right|^n} \right)^m, \quad (11)$$

where  $\beta$  and  $n$  are material-dependent parameters, and  $m = 1 - 1/n$ . Similarly, the relative permeability can be correlated to  $S_w$  according to the combined model proposed by Mualem-van Genuchten [40–42]:

$$k_{r,w} = \Theta_w^L \left[ 1 - \left( 1 - \sqrt[m]{\Theta_w} \right)^m \right]^2, \quad (12)$$

where  $L$  is a material-dependent parameter [41]. Here, as the porous matrix was supposed to be rigid during the absorption transient, the water retention curve described by Eq. 11 was assumed as the same for both imbibition and draining. In case of swelling media (*e.g.* soil science), instead, the model should account for possible hysteresis, thus different values of  $\beta$ ,  $L$  and  $n$  should be considered for the imbibition and draining.

As commonly assumed in wicking phenomena [1], the air pressure was considered constant within the porous matrix. Thus, referring to Eq. 10 and recalling that  $\Theta_w = S_w$  is assumed here, it can be written:

$$\frac{\partial S_w}{\partial t} = \frac{\partial S_w}{\partial p_c} \frac{\partial p_c}{\partial t} = -\frac{\partial S_w}{\partial p_c} \frac{\partial p_w}{\partial t}. \quad (13)$$

Eq. 13 can be then substituted in Eq. 9, which becomes:

$$-\rho_w \phi \frac{\partial S_w}{\partial p_c} \frac{\partial p_w}{\partial t} + \nabla \cdot \left[ -\rho_w \frac{Kk_{r,w}(S_w)}{\mu} (\nabla p_w + \rho_w g) \right] = -f. \quad (14)$$

The model proposed in Eqs. 11, 12 and 14 can be used to describe the capillary suction in a hydrophilic porous media once its absolute permeability to the wetting fluid  $K$  (see section 2.2.2) and the material-dependent parameters  $\beta$ ,  $L$  and  $n$  are known. Thus, the software COMSOL Multiphysics<sup>®</sup> was used to calibrate  $L$ ,  $n$  and  $\beta$  on the basis of the data obtained from the vertical wicking experiments. The experimental setup described in section 2.2.1 was represented by a 1-dimensional geometry (see Fig. 5A). The pressure field  $p_w$  was computed by solving Eq. 14, and it was then used to evaluate the time and space evolution of  $S_w$  by Eqs. 10 and 11. The position of the water front  $h_t$  at the time  $t$  was evaluated by analysing the saturation curve. At the water inlet, a fixed-pressure boundary condition  $p_w = p_0$  was used, where  $p_0 = 0$  Pa is the relative ambient pressure; no-flow condition was applied at the outlet (see Fig. 5A). Coherently with the boundary conditions, the initial values of the pressure field

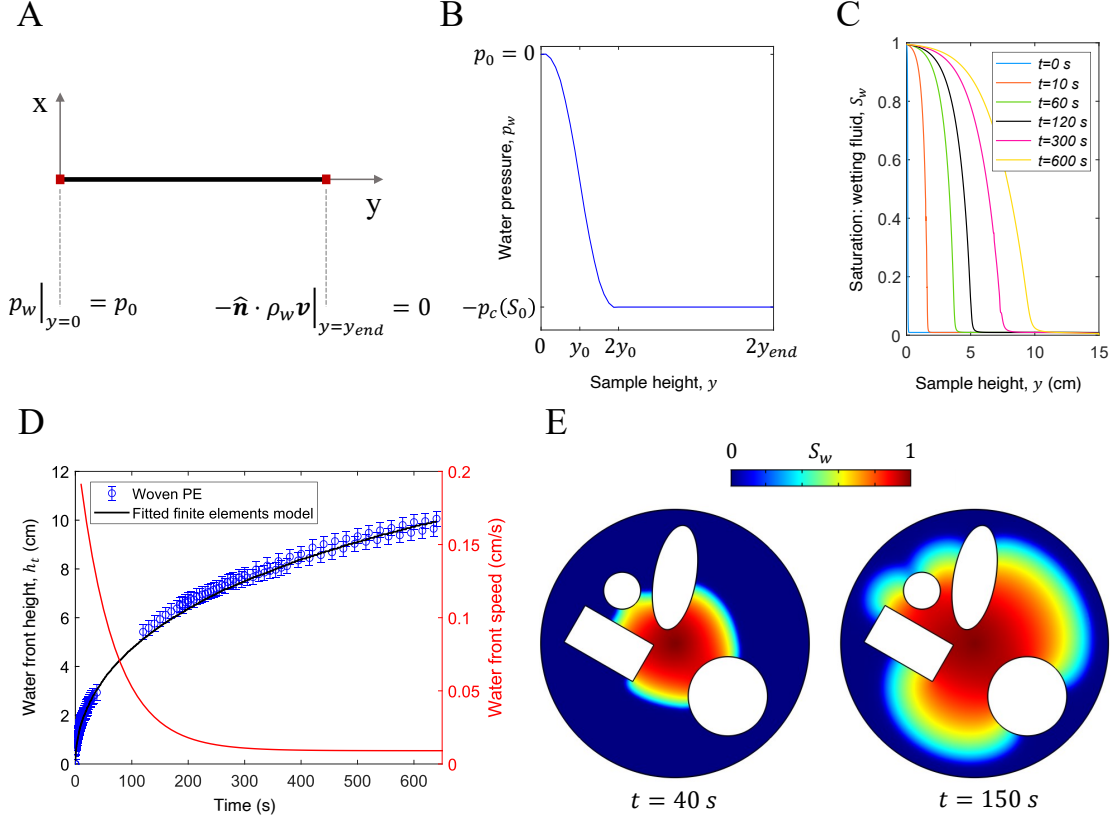


Figure 5: **Modelling of water wicking.** (A) Schematic of the finite elements 1-dimensional model used to estimate the Van Genuchten parameters. The picture reports the boundary conditions used in the simulations at the beginning ( $y = 0$ ) and at the end ( $y = y_{end}$ ) of the simulation domain. (B) Qualitative representation of the assigned initial values of the pressure fields in the domain, with  $p_0 = 0$  atm the relative ambient pressure and  $S_0 = 0.01$  the initial saturation of the fabric, necessary to improve the numerical stability. A transition zone around  $y_0 = 1$  mm is required to grant numerical stability and an initialisation coherent with the left boundary conditions. (C) Profile of the wetting fluid saturation  $S_w$  at different instants obtained from the 1-dimensional finite elements simulation. The results represent the motion of water within the porous domain during the wicking transient (*i.e.* the height of the water front  $h_t$  and the front thickness). (D) The data obtained from the vertical wicking tests (blue circles) are used to estimate the material dependent parameters  $L$ ,  $\beta$  and  $n$  of Eq. 16 for the woven PE fabric (solid black line). The average speed of water (solid red line) was approximated as the numerical derivative of the water front height with respect to time. The low water speed within the fabric allows to neglect convection in the transient heat-transfer simulation. (E) The model parameters calibrated from the wicking experiments can be used to study the wicking transient in 2-D geometries, where – for example – hydrophobic zones can be implemented as impermeable holes. Notice that the circular sample shown is supposed to wick water from the center.

were evaluated using a step function:

$$p_w(y) = \begin{cases} p_0 & \text{if } y \leq y_0 \\ p_0 - p_c(S_0) & \text{if } y > y_0, \end{cases} \quad (15)$$

where  $y$  is the vertical coordinate,  $y_0 = 1$  mm the assumed initial height of the water front,  $S_0 = 0.01$  the assumed initial saturation of water in the textile (necessary to improve the numerical stability [43]), and the relation  $p_c = p_c(S_0)$  can be obtained from Eq. 11 as a function of the material dependent parameters  $n$  and  $\beta$ . Eq. 15 was smoothed considering a transition zone  $y_0 \pm 1$  mm and continuous second order derivative. A qualitative representation of the initial values used in the 1-D simulations is reported in Fig. 5B. A few numerical assumptions were made to ease the convergence of the solver: the relative permeability of the wetting fluid  $k_{r,w}$  was constrained in the range  $10^{-3} \leq k_{r,w} \leq (1 - 10^{-3})$ ; the saturation of the wetting

fluid was limited to  $S_w \leq 0.99$  [43]; a ramp function  $r$  with a transition zone equal to  $\omega = 0.8$  and continuous second derivative was added to the denominator of Eq. 11, namely [44]:

$$\Theta_w = \left( \frac{1}{1 + \left| \beta \cdot r \left( \frac{p_c}{\rho_w g} \right) \right|^n} \right)^m. \quad (16)$$

At this stage, the effect of evaporation on the time dependent position of the water front was neglected, and the wetting fluid density  $\rho_w = 997 \text{ kg} \cdot \text{m}^{-3}$ , viscosity  $\mu_w = 10^{-3} \text{ Pa} \cdot \text{s}$  and thermal conductivity  $k_w = 0.6 \text{ W}/(\text{m} \cdot \text{K})$  considered as constant.

The simulations were performed with a time-dependent solver for 640 s, using an adaptive time-step. The position of the water front at a given time-step was evaluated as the first position with respect to the imbibition point, which

is referenced as  $y = 0$ , reaching a saturation  $S_w < 0.05$ .

### 3.1.2. Results

The results of the numerical model of the wetting process are reported in terms of the saturation profile  $S_w$  within the 1-D porous medium at different instants (see Fig. 5C). At the beginning of the simulation ( $t = 0$  s, solid blue line) the porous material is dry, namely  $S_w = 0$ , while its bottom end is put in contact with the reservoir, *i.e.*  $S_w|_{y=0} = 0.99$ . As the simulation proceeds, the water front advances, modifying the saturation profile within the textile according to the wicking parameters. The best-fit parameters evaluated by comparing the experimental and the numerical results are  $L = 0.324$ ,  $\beta = 6.7192 \text{ m}^{-1}$  and  $n = 7.79$ . The resulting curve (see Fig. 5D, solid black line) fits the experimental data with a R-Squared value of 0.997. The speed of water within the textile during wicking was approximated with the time derivative of the water front speed (see Fig. 5D, solid red line), as commonly done under the sharp-front approximation [1]. The water speed tends to decrease during the transient, as the capillary pressure is balanced by increased losses due to viscous friction. The maximum value of water speed is observed at the beginning of the wicking transient, with a peak of approximately  $2 \cdot 10^{-3} \text{ m/s}$ . This result allows to neglect the advective contribution to heat transfer. The obtained values of  $L$ ,  $\beta$  and  $n$  enable to extend the analysis from 1-D to more complex 2-D or 3-D systems, which could not be investigated relying on purely analytical models. As an example, Fig. 5E shows a 2-D circular textile sample which wicks water from its center (see also Supplementary Video 1). The non-hydrophilic areas (*e.g.* holes) within the domain alter the water transport, but can be easily implemented with a finite elements model with the same mathematical formulation used for its 1-dimensional counterpart.

## 3.2. Evaporation

### 3.2.1. Methods

The evaporation of the wetting fluid from the porous medium was modelled according to the Hertz-Knudsen equation [45, 46]:

$$\dot{m}_{ev} = E\phi\sqrt{\frac{M_w}{2\pi R}}\left(\frac{p_{sat}(T_w)}{\sqrt{T_w}} - RH\frac{p_{sat}(T_v)}{\sqrt{T_v}}\right), \quad (17)$$

where  $T_w$  is the temperature of the evaporating liquid,  $T_v$  is the vapour temperature,  $R_g$  is the universal gas constant,  $M_w$  is the molecular weight of water,  $p_{sat}$  is the saturation pressure at a given temperature,  $E$  is dimensionless evaporation rate, which depends on environmental conditions (*i.e.* the vapour stratification above the evaporating liquid) [45], and  $\phi$  is the porosity of the porous surface. Notice that the Hertz-Knudsen equation here includes  $\phi$  to take into account the reduced evaporating surface with respect to a corresponding free liquid surface. In the present work, the evaporating liquid and its vapour

were assumed at thermal equilibrium [46], thus  $T_w = T_v$ . The saturation pressure was evaluated according to the Antoine's equation:

$$p_{sat} = \frac{101325}{760} \cdot 10^{A_A - B_A/(C_A + T)}, \quad (18)$$

where  $A_A = 8.07131$ ,  $B_A = 1730.63^\circ\text{C}$  and  $C_A = 233.426^\circ\text{C}$  are component-specific coefficients for water,  $T$  is the considered temperature expressed in  $^\circ\text{C}$ . Since the output of the Antoine's law is expressed in mmHg, a conversion coefficient was introduced to express  $p_{sat}$  in Pa.

The evaporation rate from a surface at temperature  $T$  is related to the ambient conditions through Eq. 17, which however requires to evaluate the evaporation rate constant  $E$ , a function of setup-specific conditions and reported to span several order of magnitudes [47]. Thus, the value of  $E$  corresponding to the experimental setup and test conditions reported in section 2.3.1 was calibrated by a finite element model built in the COMSOL Multiphysics® software. The model, which implicitly couples heat and mass transfer, was employed to iteratively change the value of  $E$  until the obtained numerical temperature trends matched those reported in Fig. 3B. With respect to experiments, the 2-D simulation domain and its boundary conditions (see Fig. 6A) were modelled to mimic the experimental setup described in section 2.3.1. Coherently with the estimation of the van Genuchten's parameters (see 3.1.2) and given the narrow range of temperatures experimentally observed (see Fig. 3B), the thermophysical properties of water used to model the mass transfer were considered as constant, while the polynomials used to compute the temperature dependent properties of air and water at the heat transfer interface are reported in Supplementary Note 4. At this stage, the effect of radiative heat transfer was neglected. As described in section 3.1.1, wicking dynamics was modelled by Eq. 14 with similar assumptions: the outmost circular boundary was considered as impermeable; a point-wise injection well condition was imposed at the center of the circular domain (with  $p_w = p_0$ ) to simulate the wetting by a water droplet; the horizontality of the setup allowed to neglect the effect of gravity. Furthermore, the sink term was evaluated from Eq. 17 and suppressed if the water saturation was lower than  $S_0$  (see Fig. 6A), namely:

$$-f = \begin{cases} 0 & \text{if } S_w \leq S_0 \\ -\dot{m}_{ev}/d_z & \text{if } S_w > S_0, \end{cases} \quad (19)$$

where  $d_z$  is the thickness of the textile, evaluated as described in section 2.2.1. The initial values of the pressure field were taken according to the step function:

$$p_w(x, y) = \begin{cases} p_0 & \text{if } x^2 + y^2 \leq R_0 \\ p_0 - p_c(S_0) & \text{if } x^2 + y^2 > R_0, \end{cases} \quad (20)$$

where  $x$  and  $y$  are the two horizontal spatial coordinates,  $R_0 = 1 \text{ mm}$  is the size of the injection well (namely the



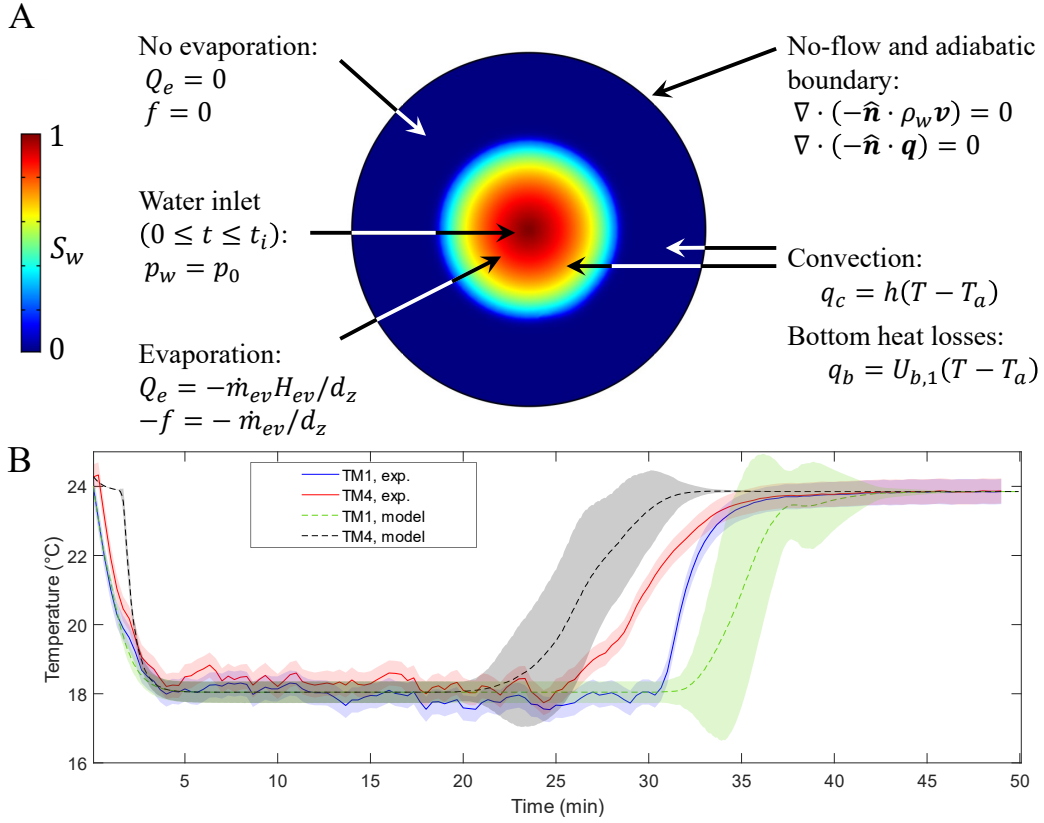


Figure 6: **Modelling of water evaporation from the porous fabric.** (A) Schematic of the 2-dimensional simulation setup and its boundary conditions for the evaporation process. The sink term  $-f$  and the volumetric heat flux  $Q_e$  were only applied where  $S_w > S_0$ , while the boundary convective heat flux  $q_c$  and thermal losses  $q_b$  were considered over the entire domain. (B) Comparison between the experimental (blue and red solid lines) and modelled (green and black solid lines) temperature transients used to validate the evaporation model and fit the evaporation coefficient  $E$  in Eq. 17. The solid and dashed lines represent the average values and their shaded contour their uncertainty (see Supplementary Note 1).

size of the zone considered wet at the beginning of the simulation) and  $S_0 = 0.01$  is the assumed initial saturation in the domain.

The energy balance equation was used to model heat transfer in the computational domain:

$$(\rho c_p)_{eff} \frac{\partial T}{\partial t} + \nabla \cdot \mathbf{q} = Q, \quad (21)$$

considering:

$$\begin{aligned} (\rho c_p)_{eff} &= \phi \rho_m c_{p,m} + (1 - \phi) \rho_F c_{p,F}, \\ \mathbf{q} &= -k_{eff} \nabla T, \\ k_{eff} &= \phi k_m + (1 - \phi) k_F, \end{aligned} \quad (22)$$

where the subscripts  $m$  and  $F$  respectively refer to the porous matrix and the fluid domain,  $T$  is the moist fabric temperature,  $c_p$  is the specific heat at constant pressure,  $\mathbf{q}$  is a general boundary heat flux (expressed in  $\text{W}/\text{m}^2$ ),  $Q$  is the general source/sink term (expressed in  $\text{W}/\text{m}^3$ ),  $k_m$  and  $k_F$  are the thermal conductivities of the porous matrix and of the fluid domain, respectively. Given the low velocity of the water in the domain, the velocity field

$u$  was set to 0 (see section 2.2.2 for further details). The thermophysical properties of the fluid within the porous medium domain  $\rho_F$ ,  $c_{p,F}$  and  $k_F$  were obtained by averaging those of water and air based on the local saturation of the pores (e.g. the density of fluid domain was computed as  $\rho_F = S_w \rho_w + S_{nw} \rho_{nw}$ ), while the thermal properties of the porous matrix were experimentally characterised and considered as constant.

The volumetric heat flux due to evaporation  $Q = Q_e$  (see Fig. 6A) was evaluated as:

$$Q_e = \begin{cases} 0 & \text{if } S_w \leq S_0 \\ -\dot{m}_{ev} H_{ev} / d_z & \text{if } S_w > S_0, \end{cases} \quad (23)$$

where  $H_{ev} = 2276 \text{ kJ/kg}$  is the enthalpy of vaporisation of water considered as constant. Further details on the evaluation of the boundary heat fluxes due to convection  $\hat{n} \cdot \mathbf{q} = q_c$  and to the boundary heat losses through the bottom side of the setup  $\hat{n} \cdot \mathbf{q} = q_b$ , where  $\hat{n}$  is the versor perpendicular to a boundary surface, are reported in Supplementary Note 5. To mimic the experimental imbibition and subsequent drying of the textile, the simulation was performed as a combination of three consecutive, time-



dependent computational steps. First, the pressure field in the domain represented in Fig. 6A was equilibrated by simulating the water transport model only for 0.5 seconds, neglecting the evaporation of the fluid to grant numerical stability. Then, the simulation was carried out while coupling the heat and mass transfer physics until  $t = t_i$ , where  $t_i$  is the time at which the overall volume of water wicked by the textile  $V_w$  matched the volume of the droplet deposited during the experiment, namely  $V_w = (0.25 \pm 0.02)$  ml. The volume of water wicked by the textile at a given time-step was evaluated as:

$$V_w = \iint_{A_s} (\delta S_w d_z \phi) dA_s, \quad (24)$$

being

$$\delta = \begin{cases} 0 & \text{if } S_w \leq S_0 \\ 1 & \text{if } S_w > S_0, \end{cases} \quad (25)$$

and  $A_s$  the upper surface of the circular sample. Third, the drying process was simulated until  $t = 2000$  s while removing the pressure constraint at the center of the textile, namely after stopping the water uptake.

### 3.2.2. Results

The experimental data presented in Fig. 3B were used to evaluate the evaporation constant  $E$  in Eq. 17, which is a characteristic of the experimental testing conditions. First, the wicking model was used to estimate the time of the wicking transient  $t_i$ , namely the time required to a 2-dimensional circular textile sample to be wicked by a volume of water equal to the droplet used in the experiments. Note that the experimental procedure prescribed to lay the water droplet on a textile previously deposited on the substrate surface was described in section 2.3.1 (see Figs. 3A). As a result, the absorption and spread of water was not only due to pure wicking, as assumed in the model, since the pressure field was influenced by the weight of the textile itself. Thus, the modelled imbibition time  $t_i$  is a simplified numerical counterpart of the absorption phenomenon observed in the experiment. The imbibition transient was simulated using the values of the retention parameters  $L$ ,  $\beta$  and  $n$  previously evaluated and, as discussed in section 2.2.2, the effect of water evaporation during the wicking transient was neglected. With a simulated imbibition time  $t_i = 58.7$  s, the volume of water wicked by the textile was  $V_w = 0.243$  ml, coherent with the volume of the water droplet used for the experiment  $(0.25 \pm 0.02)$  ml. It is worth to point out that the width of the transition  $\omega = 0.8$  of the ramp function  $r$  used in Eq. 16 affects the profile of  $S_w$  during the wicking transient and, thus,  $t_i$ . However, as discussed in Supplementary Note 6, its effect on the estimated imbibition time  $t_i$  is negligible.

To evaluate the evaporation constant  $E$ , the experimental temperature curves of the thermistors TM1 and

TM4 were compared with the results of simulation. The low temperature difference between the drying textile and the ambient resulted in an average Rayleigh number  $Ra < 10^5$ , thus below the range of validity reported in Eq. S15 to evaluate the convection coefficient  $h$ . As a consequence,  $h$  was estimated as  $h = (6.0 \pm 0.2)$  W/(m<sup>2</sup>K), which considered the effect of the forced ventilation in the laboratory environment and is coherent with the minimum convection coefficient reported for still air conditions, approximately 5 W/(m<sup>2</sup>K) [48]. The best fitting curves were obtained for  $E = 0.079$ , the results are shown in Figs. 6B-C. The computed temperature at the center of the sample (see Fig. 6B, dashed green line) recovers accurately the experimental one (solid blue line), while the discrepancy between TM4 (solid red line) and the respective computed value (dashed black line) could be ascribed to both experimental and theoretical inaccuracies, for instance: the manual deposition of both the water droplet and the textile sample on the support; the constraint imposed to the evaporation rate by Eq. 19 and 23, which limits the evaporation to the regions with  $S_w > S_0$ . An important parameter to determine the efficiency of the moisture transport of textiles is the wet-to-dry time: in the considered testing conditions, this was experimentally estimated as  $(29.4 \pm 0.5)$  min, which is in good agreement with the results of the simulation, namely  $(34 \pm 2)$  min.

In conclusion, it is worth to point out that evaporation is a particularly complex phenomenon, as it strongly depends on several properties of the boundary layer above the evaporating surface: concentration of water vapour, interfacial temperature, air-flow velocity, pressure and size of the evaporating surface. However, the proposed heat and mass transfer model was able to recover the experimental behaviour of the tested material by employing a single, condition-specific scaling coefficient  $E$ .

### 3.3. Radiation

#### 3.3.1. Methods

For the semi-transparent fabric, it holds [48]:

$$\alpha_f(\lambda) + \tau_f(\lambda) + r_f(\lambda) = 1, \quad (26)$$

where  $\alpha_f$ ,  $\tau_f$ ,  $r_f$  are respectively the absorption, transmission and reflection coefficients for a given wavelength  $\lambda$  and the subscript  $f$  refers to the fabric. The surface of the heater is modelled as an opaque medium, thus:

$$\alpha_h(\lambda) + r_h(\lambda) = 1, \quad (27)$$

where the subscript  $h$  refers to the surface of the heater. According to the Kirchhoff's law, the wavelength-dependent absorptivity and emissivity were assumed equal for both the fabric and the heater [48], namely:  $\epsilon_{f/h}(\lambda) = \alpha_{f/h}(\lambda)$ . As reported in section 2.4.1, the experimental evaluation of the optical properties of the semi-transparent fabric was done in the wavelength range from  $\lambda_i = 0.25$   $\mu\text{m}$  to  $\lambda_e = 2.5$   $\mu\text{m}$ , and from  $\lambda_i = 2.5$   $\mu\text{m}$  to  $\lambda_e = 20$   $\mu\text{m}$ . In

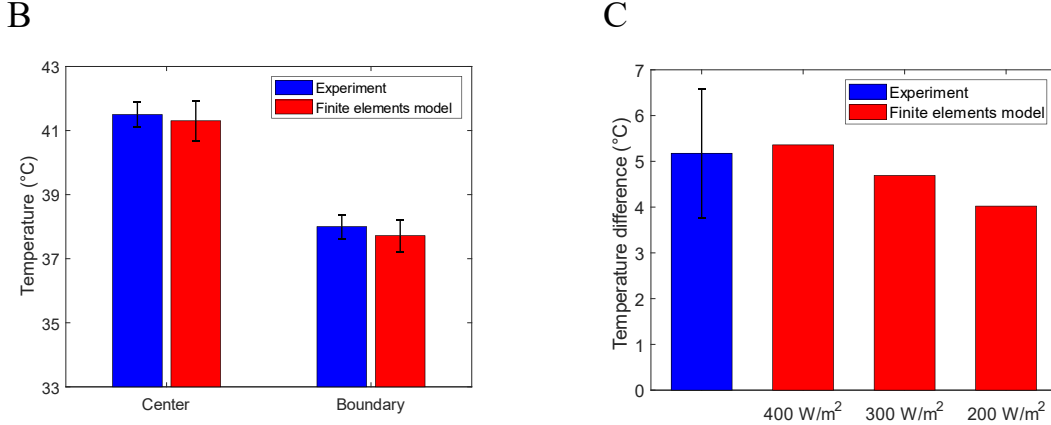
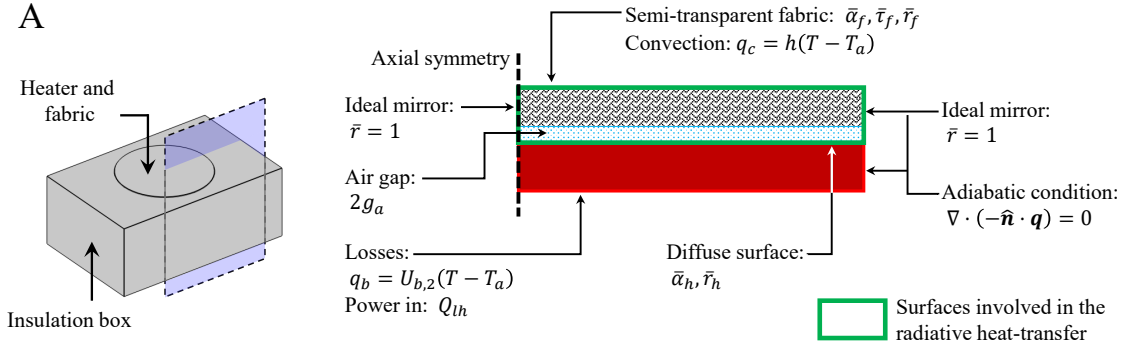


Figure 7: **Modelling of the radiative heat transfer properties.** (A) Schematics of the 2-dimensional simulation setup, highlighting the surfaces involved in the radiative heat transfer (solid green lines). (B) Comparison between the measured and computed temperatures at the center and boundary of the specimen at the steady state of indoor test, considering the covered configuration. (C) Comparison between the measured and computed temperature difference between the covered and uncovered setups in the outdoor configuration. The experimental temperature difference, evaluated from the temperature trends in Fig 4C, was obtained as the time-average of the last 150 min recorded. To evaluate the effect of the varying solar irradiance (see panel B), the results were computed for three different values of  $I_{rr}$ , showing a general good agreement with the measurement.

these ranges, the average optical properties can be computed as [49]:

$$\bar{\alpha}_f = \frac{\int_{\lambda_i}^{\lambda_e} \alpha_f(\lambda) I_{rr}(\lambda) d\lambda}{\int_{\lambda_i}^{\lambda_e} I_{rr}(\lambda) d\lambda}, \quad (28)$$

where  $I_{rr}(\lambda)$  is the wavelength dependent incident radiation on the surface. The average transmission  $\bar{\tau}_f$  and reflection  $\bar{r}_f$  coefficients were evaluated similarly to Eq. 28.

The radiative heat transfer process in the considered experiment includes the interaction between three bodies: the opaque heater, the semi-transparent textile and the ambient, where the latter is considered as a black-body. Considering an external incident radiative heat-flux  $I_{rr}(\lambda)$  and assuming the air gap between the heater and the fabric as a non-participating medium, the heat absorbed by the fabric  $-\hat{\mathbf{n}} \cdot \mathbf{q} = q_{r,f}^{ext}$ , expressed in  $\text{W}/\text{m}^2$ , can be computed

as:

$$q_{r,f}^{ext} = \left( \bar{\alpha}_f + \sum_{n=1}^{\infty} \bar{\tau}_f \bar{\alpha}_f \bar{r}_f^{n-1} \bar{r}_h^n \right) \int_{\lambda_i}^{\lambda_e} I_{rr}(\lambda) d\lambda, \quad (29)$$

where  $I_{rr}$  was evaluated by hemispheric integration of the Planck's black body radiation  $E_r(T, \lambda)$  (expressed in  $\text{W}/(\text{m}^3\text{sr})$ ) on the solid angle  $\theta$  in the case of indoor conditions (namely  $I_{rr}(\lambda) = \int_0^\pi E_r(T_a, \lambda) d\theta$ ), and  $I_{rr}(\lambda) = \int_0^\pi E_r(T_{sky}, \lambda) d\theta$  in the case of outdoor conditions,  $I_{rr}(\lambda) = \text{AM1.5}$  for solar radiation (see Supplementary Note 7 for further details on the evaluation of the sky temperature  $T_{sky}$  and  $E_r$ ). The summation in Eq. 29 considers the share of incoming radiation transmitted by the fabric, reflected by the substrate, and absorbed by the fabric. The process is iteratively repeated (*i.e.*  $n > 1$ ) due to the reflection index of the fabric, and usually becomes negligible for  $n \geq 6$ . Similarly, the specific heat flux absorbed by the heater from an incident

external source can be evaluated as:

$$q_{r,h}^{ext} = \left( \bar{\tau}_f \bar{\alpha}_h + \sum_{n=1}^{\infty} \bar{\tau}_f \bar{\alpha}_h \bar{r}_f^n \bar{r}_h^n \right) \int_{\lambda_i}^{\lambda_e} I_{rr}(\lambda) d\lambda. \quad (30)$$

The specific heat fluxes absorbed by the fabric  $q_{r,f}^{int}$  and by the heater  $q_{r,h}^{int}$  due to the mutual infrared heat transfer, considering the two surfaces as parallel plates with unitary view factor, was evaluated as:

$$q_{r,f}^{int} = \bar{\alpha}_f \left( \sum_{n=0}^{\infty} \bar{\alpha}_h \bar{r}_f^n \bar{r}_h^n \right) \int_0^{\pi} \int_{\lambda_i}^{\lambda_e} E_r(T_h) d\lambda d\theta + \bar{\alpha}_f \bar{r}_h \left( \sum_{n=0}^{\infty} \bar{\alpha}_f \bar{r}_f^n \bar{r}_h^n \right) \int_0^{\pi} \int_{\lambda_i}^{\lambda_e} E_r(T_f) d\lambda d\theta, \quad (31)$$

and

$$q_{r,h}^{int} = \bar{\alpha}_h \left( \sum_{n=0}^{\infty} \bar{\alpha}_f \bar{r}_f^n \bar{r}_h^n \right) \int_0^{\pi} \int_{\lambda_i}^{\lambda_e} E_r(T_f) d\lambda d\theta + \bar{\alpha}_h \bar{r}_f \left( \sum_{n=0}^{\infty} \bar{\alpha}_h \bar{r}_h^n \bar{r}_f^n \right) \int_0^{\pi} \int_{\lambda_i}^{\lambda_e} E_r(T_h) d\lambda d\theta. \quad (32)$$

The software COMSOL Multiphysics<sup>®</sup> was used to validate the radiative heat transfer model and to fit the thermal properties of the heater used for the experiments. A schematics of the simulation setup is reported in Fig. 7A. Eq. 21 was solved in the computational domain to determine the surface temperature of the heater. Further details on the implementation of boundary heat fluxes and on the effect of  $S_w$  on the optical properties of the fabric are reported in Supplementary Note 7.

### 3.3.2. Results

The comparison between the measured and computed temperatures at the steady state for the indoor experiment is reported in Fig. 7B. The experimental results and the theoretical predictions are in good agreement and comparable within their uncertainty. The simulation results show the effect of the air gap between the heaters surface and the fabric on the substrate temperature: the local surface temperature varies of approximately 1.3 °C and 1 °C, respectively, at the center and boundary of the setup, varying the air gap thickness in the range  $71 \mu\text{m} \leq g_a \leq 212 \mu\text{m}$ . Therefore, an accurate evaluation of the thermal contact between the fabric and its substrate is crucial to obtain reliable numerical results.

Fig. 7C compares the theoretical and experimental results in outdoor conditions. The temperature difference between the covered and uncovered setups was evaluated by averaging the experimental results between minutes 160 and 300, where the solar irradiance varied between 370 W/m<sup>2</sup> and 100 W/m<sup>2</sup> (blue bar). Since the temperature difference was more scattered with respect to the indoor test, simulations were performed considering three different values of solar irradiance  $I_{rr} = [200, 300, 400]$

W/m<sup>2</sup>, while the ambient temperature and external convection coefficient were fixed at  $T_a = 17.5 \text{ °C}$  and  $h = 22.2 \text{ W/(m}^2\text{K)}$ , respectively, and the sky temperature was evaluated considering  $RH = 0.4$  (see Supplementary Note 7). The numerical result obtained are in good agreement with the experimental one, with a maximum deviation of 22% (with  $I = 200 \text{ W/m}^2$ ), coherently with the experimental uncertainty.

## 4. Discussions and Applications

The validated model could be extrapolated to show possible applications in three different scenarios: characterising the properties of an unknown material; estimating the thermal performances of a known material exposed to different working conditions; designing the optimal properties of a novel component of a target device, given specific working constraints.

The procedure presented in sections 2 and 3 belongs to the first scenario: by means of simple experimental procedures and numerical modelling, the material-dependent properties (the average porosity  $\phi$ , thickness  $d_z$ , absolute permeability  $K$ , wicking parameters  $\beta$ ,  $n$  and  $L$ , and optical properties  $\bar{\alpha}_f$ ,  $\bar{\tau}_f$  and  $\bar{r}_f$ ) and condition-specific parameters (the evaporation rate  $E$ ) of a novel woven PE material were evaluated and the model calibrated for the intended purpose. However, the procedure required several accessory simulations to provide setup-specific parameters essential to recover the experimental results: the heat transfer coefficients of the polystyrene insulations ( $U_{b,1}$  and  $U_{b,2}$ , see Supplementary Note 5 and 7, respectively), the outdoor convection coefficient ( $h_{out}$ , see section 2.4.2) and the non-homogeneous heating characteristic of the silicone heaters (see Supplementary Note 3). For the sake of clarity, the workflow of the proposed characterisation procedure was summarised in the block diagrams shown in Supplementary Figs. S2 and S3, where the setup-specific parameters are highlighted with dash-dotted contours. Evidently, if any of the condition-specific or setup-specific parameters were known *a-priori* or simplifying assumptions employed (e.g. adiabatic conditions replacing the heat transfer coefficients  $U_{b,1/2}$ ), the accessory simulations would be avoided, easing the procedure.

The second and third scenarios described are investigated in sections 4.1 and 4.2, respectively. The former presents an application-specific sensitivity analysis aimed to assess how different ambient conditions affect the thermal performances of the woven PE textile, characterised in this work, which was specifically designed for passive personal thermal management. Approaching this optimisation problem with modelling is beneficial, given the large number of variables and the strong non-linearity of the system response to the input parameters. Then, a design-oriented sensitivity analysis was employed to assess the effect of the van Genuchten's parameter on the macroscopic capillary properties of porous materials, to explore qualitatively how they affect the feasible design of a component

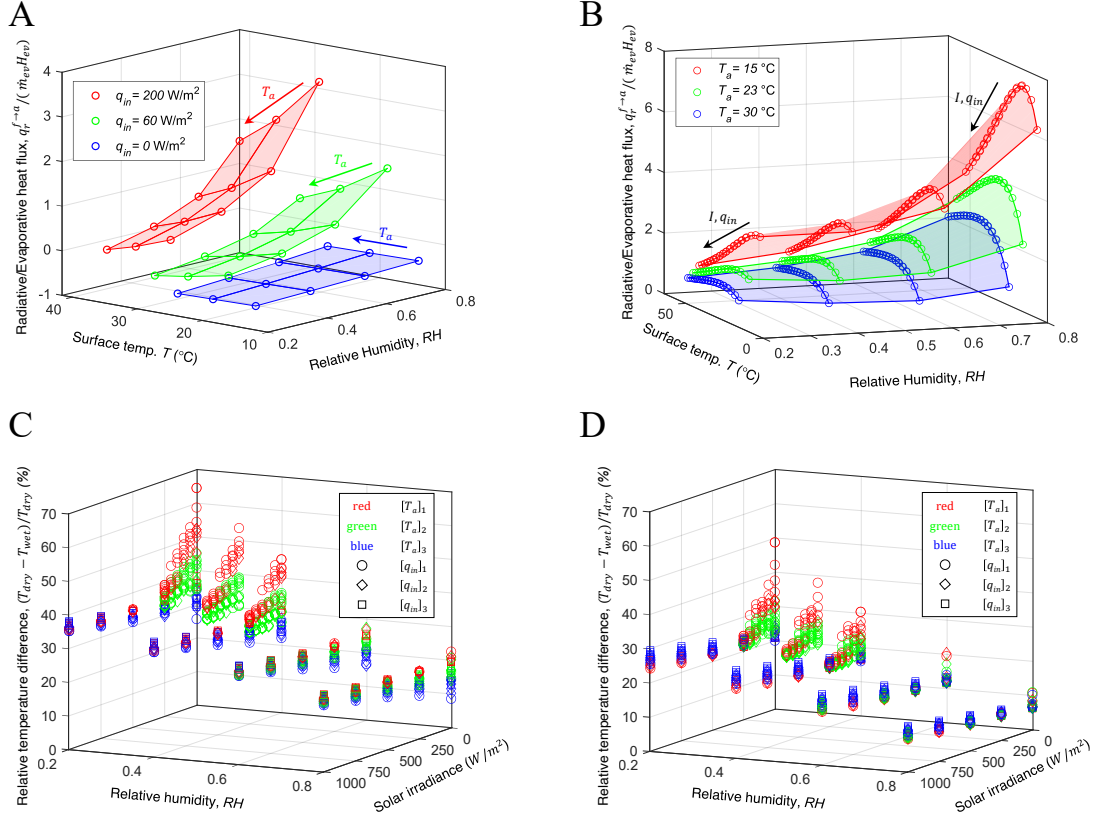


Figure 8: **Cooling performance of a PE fabric for personal passive thermal management at different ambient conditions.** (A) Analysis of the ratio between the radiative (IR) and evaporative heat fluxes from the fabric top surface in indoor conditions. Different values of relative humidity ( $RH$ ), ambient temperature ( $T_a$ ) and supplied heat flux ( $q_{in}$ ) were tested. For most of the configurations simulated, evaporation was found to be the principal cooling mechanism. (B) Analysis of the ratio between the radiative (IR) and evaporative heat fluxes from the fabric top surface in outdoor conditions for different environmental parameters. The simulations were performed varying the supplied heat flux in the range  $0 \text{ W/m}^2 \leq q_{in} \leq 200 \text{ W/m}^2$  and the incident solar radiation in the range  $0 \text{ W/m}^2 \leq I_{rr} \leq 1000 \text{ W/m}^2$ . Differently from the indoor configuration, the radiative heat flux prevailed over evaporative one for low values of  $T_a$  and high values of  $RH$ ,  $q_{in}$  and  $I_{rr}$ . (C) Ratio between the surface temperature of dry and wet conditions in outdoor for the considered woven PE fabric and (D) for an ideal fabric with  $\bar{\tau}_f = 1$ . The optical properties of the fabric in the UV-VIS-NIR spectrum were not changed. The simulations were performed considering three ranges for  $T_a$  and  $q_{in}$  (see Tab. 1). As expected, the average temperature of the simulated skin is lower if covered by a wet fabric, and this effect is more pronounced for high values of both  $I_{rr}$  (increased radiative heat flux) and  $RH$  (reduced evaporation).

suitable for passive devices. A representative field of application for this type of analysis is passive thermal water desalination, which relies on wicking to feed the evaporation stages: poor capillary properties limit the maximum size of the device when subject to high solar fluxes (thus high evaporation rates), hence hindering the scalability of the technology. The proposed modelling approach can be used to engineer the porous properties of the wicking materials for passive desalination, avoiding its dry-out and maximising the performances given specific boundary conditions.

#### 4.1. Case study: performance assessment of a textile for passive personal thermal management

The simulations were performed employing the setup used to validate the radiative heat transfer model in Fig. 7A. Similarly, the solutions were computed using a steady state solver, hence the wicking transient was neglected and the textile, if wet, was assumed as completely saturated by

water, namely  $S_w = 0.99$ . A few numerical assumptions were made: the supplied specific heat flux  $q_{in}$  (expressed in  $\text{W/m}^2$ ) was supposed to be homogeneously supplied by the silicone heater; both indoor and outdoor conditions were simulated considering natural convection, thus the convection coefficient  $h$  was evaluated from Eqs. S14, S15 and S16; if the lower limits of the Ra number expressed in Eq. S15 were not satisfied, the convection coefficient was assumed equal to  $h = 6 \text{ W/(m}^2\text{K)}$ ; the fitted evaporation rate  $E = 0.079$ , the enthalpy of vaporisation  $H_{ev} = 2276 \text{ kJ/kg}$  and the absolute permeability  $K = 1.7 \cdot 10^{-12} \text{ m}^2$  (see section 2.2.2) were assumed as constants.

Fig. 8A shows the ratio between the radiative (IR)  $q_r^{f \rightarrow a}$  and the evaporative heat fluxes emitted by the top surface of the wet woven PE fabric for indoor conditions. The textile surface temperature  $T$  is a fundamental parameter to evaluate the evaporative and radiative heat fluxes, thus it was represented on the left horizontal axis of Fig. 8A, although it is an output from the simulations.

	$[q_{in}]_1 : q_{in} \leq 30$	$[q_{in}]_2 : 30 < q_{in} \leq 80$	$[q_{in}]_3 : 80 < q_{in} \leq 200$
$[T_a]_1 : T_a \leq 17$	red circles, $\circ$	red diamonds, $\diamond$	red squares, $\square$
$[T_a]_2 : 17 < T_a \leq 22$	green circles, $\circ$	green diamonds, $\diamond$	green squares, $\square$
$[T_a]_3 : 22 < T_a \leq 30$	blue circles, $\circ$	blue diamonds, $\diamond$	blue squares, $\square$

Table 1: Symbols used in Figs. 8C-D to represent the tested combinations of ambient temperature  $T_a$  (expressed in  $^{\circ}\text{C}$ ) and specific input power  $q_{in}$  (expressed in  $\text{W}/\text{m}^2$ ).

Model predictions show that evaporation is the principal cooling mechanism for most of the configurations tested, while  $q_r^{f \rightarrow a}$  is limited (or even made negative for  $q_{in} = 0$ ) by the increased optical temperature of the surrounding environment  $T_{sky} = T_a$ , which determines the radiative heat transfer with the environment. However, the combination of high values of  $RH$  and surface temperature (caused by higher values of  $q_{in}$ ) might invert the trend. The results obtained for outdoor conditions (see Fig. 8B) outline an opposite situation. The curves displayed were obtained varying the supplied specific heat flux in the range  $0 \text{ W}/\text{m}^2 \leq q_{in} \leq 200 \text{ W}/\text{m}^2$  and the incident solar radiation in the range  $0 \text{ W}/\text{m}^2 \leq I_{rr} \leq 1000 \text{ W}/\text{m}^2$ . The radiative heat transfer in outdoor conditions is considerably favoured by a reduced value of  $T_{sky}$ , which is a function of humidity and ambient temperature. As a consequence, high values of  $RH$  and low values of  $T_a$  results in low evaporation rates and high IR emissions, favouring radiative over evaporative heat transfer. A direct evaluation of the user comfort level is provided by the fabric substrate temperature, namely the temperature of the fabric bottom layer directly in contact with the simulated skin. The effect of the environmental conditions on the fabric substrate temperature with  $q_{in} = 60 \text{ W}/\text{m}^2$  and  $I_{rr} = 1000 \text{ W}/\text{m}^2$ , respectively the usual metabolic rate at rest and the typical solar irradiance of a sunny summer day around noon, are shown in Supplementary Fig. S4.

The effect of different cooling capacities on the substrate temperature - which mimics the skin in personal thermal management applications - is represented in Figs. 8C-D, where the relative temperature difference between the dry and wet substrate (namely,  $(T_{dry} - T_{wet})/T_{dry}$ ) in outdoor conditions was represented as a function of the ambient humidity and solar irradiance. In particular, Fig. 8C was obtained considering the optical properties of the proposed woven PE fabric (see Tab. S2), while Fig. 8C with the ideal optical properties in the IR spectrum which maximise its radiative cooling performances,  $\bar{\tau}_f = 1$ . Note that both the analysis were performed considering the optical properties of the fabric in the UV-VIS-NIR spectrum in Tab. S2. To simplify the visualisation of the obtained data, they are divided into three ranges of ambient temperature and input heat flux. The symbols and colouring code used are summarised in Tab. 1.

As expected, the average temperature of the substrate surface is always lower if covered by a wet fabric (see Fig. 8C) despite presenting worse optical properties. The relative temperature difference remains within 20% for the

lowest evaporation rates (namely,  $RH = 0.8$ ), regardless the other ambient conditions, and progressively increases for lower values of  $RH$ . The largest relative differences, with a peak value of approximately 67%, are obtained for low values of ambient temperature, relative humidity, specific input heat flux and solar irradiance, coherently with the previous analysis of the cooling fluxes. Note that, in this condition, the surface temperature of the substrate is lower than  $10^{\circ}\text{C}$  (see Fig. 8B), therefore large relative differences correspond to low absolute deviations. However, it is worth to point out that those optimal parameters for a surface temperature decrease correspond to an environmental condition where, generally, cooling is not required for personal thermal management. Nevertheless, even considering an ideally transparent porous textile (namely  $\bar{\tau}_f = 1$ ), evaporation plays a crucial role (see Fig. 8D): when exposed to a solar irradiance of  $1000 \text{ W}/\text{m}^2$ , the wet textile was on average 11% and 27% colder with respect to the dry ideal fabric at  $RH = 0.8$  (lower evaporation rate) and  $RH = 0.2$  (higher evaporation rate), respectively.

#### 4.2. Case study: passive thermal desalination

A sensitivity analysis was employed to evaluate the effects of the capillary properties on the performances of a porous component of a typical solar-powered passive desalination devices (see Refs. [8, 9, 50]) in a given working condition. The component investigated (see Fig. 9A) consists in a rectangular hydrophilic porous layer used to wick salt-water from a reservoir and supply the distillation device. As the aim of the technology is to maximise the amount of distilled water produced per unit energy, a straight-forward approach would be to increase the size of the component. However, the generated vapour flux has to be balanced by the capillary water flux provided by the porous medium, which might not be large enough to sustain a continuous evaporation process throughout the entire surface.

Here, the setup was subject to a constant specific input heat flux  $q_{in} = 215 \text{ W}/\text{m}^2$ , while the van Genuchten's parameters and the width  $w$  of the rectangular evaporator were varied in the ranges  $\beta = (6 : 9) \text{ 1/m}$ ,  $n = [3, 8, 12]$  and  $w = (3 : 2 : 11) \text{ cm}$  to assess the percentage of wet surface achieved at the steady state, namely:

$$A_{wet} = \frac{100}{A_s} \iint_{A_s} \delta dA_s, \quad (33)$$



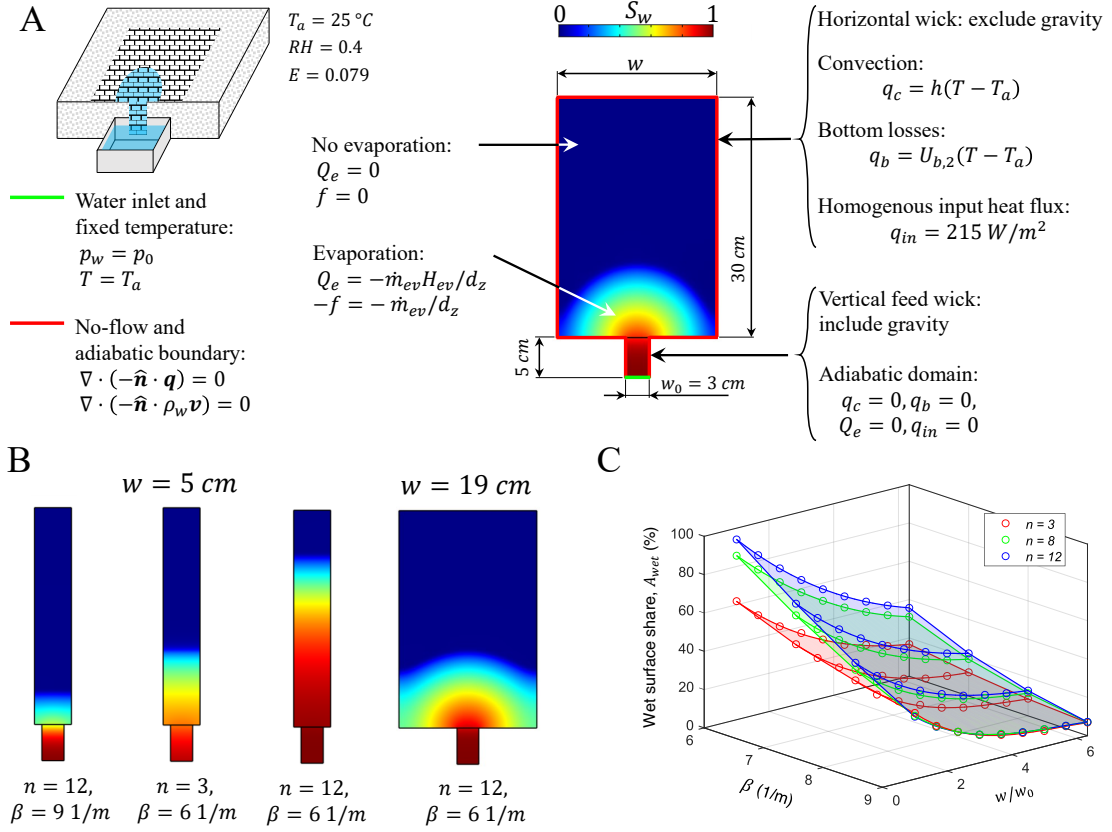


Figure 9: **Design-oriented sensitivity analysis of an hydrophilic fabric for passive thermal desalination.** (A) Schematics of the simulation setup and the employed boundary conditions. The setup represents a typical porous hydrophilic component of passive devices for water desalination. The component is used to adsorb salt-water from a reservoir, and feed a distillation device (or directly evaporate it) under solar light. (B) Steady states ( $t = 15 \cdot 10^3\text{ s}$ , see Supplementary Video 2) obtained varying the values of the van Genuchten's parameters or the width of the component  $w$ . Reducing  $\beta$  and increasing  $n$  results in a higher share of wet surface  $A_{wet}$ , thus to higher efficiency of the component. (C) Sensitivity analysis to assess the relationship between the van Genuchten's parameters  $\beta$  and  $n$ , the aspect ratio of the component  $w/w_0$  and the share of wet surface  $A_{wet}$ . Note that the simulations were performed considering distilled water.

being  $\delta$  defined in Eq. 25,  $A_s$  the total surface of the component (vertical wick included). The effect of the parameter  $L$  was not evaluated, as the results of a preliminary sensitivity analysis of imbibition highlighted how its effect was negligible on the transient (see Supplementary Note 8). The hydrophilic layer was assumed to be fabricated with the woven PE textile, characterised in sections 2 and 3, placed on an insulating polystyrene box, tested in indoor conditions and constantly wicking distilled water from a reservoir, which evaporated from the fabric surface in open air ( $E = 0.079$ ). The ambient conditions were set to  $T_a = 25^\circ\text{C}$  and  $RH = 0.4$ . The temperature of the reservoir was supposed as equal to the ambient temperature  $T_a$ . The length of the evaporator ( $30\text{ cm}$ ) and the size of the vertical fabric stripe (width  $w_0 = 3\text{ cm}$  and length  $5\text{ cm}$ ) connecting the water reservoir with the evaporator were assumed as constant. The fabric was supposed to be initially saturated and in thermal equilibrium with the surrounding environment; the drying process was simulated with a time-dependent solver for  $15 \cdot 10^3\text{ s}$ , when the steady state was reached (see Supplementary Video 2). An exhaustive description of the boundary conditions

employed can be found in Fig. 9A. As the aim was to analyse the effects of the capillary properties rather than perform an accurate design optimisation, a few assumptions were made: the effects of salinity were neglected; the average IR transmittance of the dry fabric was neglected, thus  $\bar{r}_f = 1 - \bar{\alpha}_f$  with  $\bar{\alpha}_f = 0.42$  as reported in Tab. S2; the vertical stripe was assumed as ideally insulated, thus no heat and evaporation losses were considered.

The effect of the van Genuchten's parameters  $n$  and  $\beta$  on the obtained share of wet surface  $A_{wet}$  at the steady state is shown in Fig. 9B-C. Lower values of  $\beta$  and higher values of  $n$  increased the capillary properties of the porous material, resulting in a larger front size (see Supplementary Note 8) and higher values of  $A_{wet}$ ; however, the effect of  $n$  was determinant only for low values of  $\beta$ . On the other hand, the use of higher aspect ratios  $w/w_0$  resulted in lower values of  $A_{wet}$  for all the values of the parameters tested, thus in a potentially lower distillation efficiency of the device. As a consequence, the design process of such components should consider the feasible capillary properties of the available porous materials, the size of the evaporating surface and the capacity of capillary water supply (which



depends on  $w_0$  and the height of the evaporator with respect to the reservoir) to obtain an efficient device. The comprehensive model could also be used to evaluate the time required to reach the steady state for a given working condition (here approximately  $10^4$  s for all the configurations tested). Clearly, the results presented were obtained for a given working condition: different input heat fluxes, ambient conditions and evaporation rates would result in different values of  $A_{wet}$ . However, the general trends discussed confirm the crucial role of a comprehensive model for evaluating the optimal design if wicking, evaporation, and heat transfer in porous media are involved.

## 5. Conclusions

This work presents a comprehensive heat and mass transfer model and an experimental procedure which aimed to characterise and simulate the water wicking and evaporation in capillary porous media in a systematic and self-consistent way. After calibrating and validating this model, we have envisioned and explored three different scenarios for its application, which may be of interest in the broad field of sustainable devices for water-energy nexus. In particular, sections 2 and 3 combined experimental and modelling techniques to characterise the material-dependent properties of a novel woven PE textile; the thermal performances obtained from the experimental investigation and the numerical modelling were analysed both indoor and outdoor to retrieve conditions-specific parameters and to validate the model. Then, in section 4 the focus was set on the cooling performances of the characterised fabric: the proposed model was used to estimate the effects of the ambient on the shares of radiative and evaporative heat fluxes. The objective was to determine which heat transfer mechanism prevails in a given working condition, outlining some guidelines for the rational design of novel materials for personal thermal management. Finally, the model was used to perform a sensitivity analysis to assess the effects of the van Genuchten's parameters on the capillary properties, with the intent to provide an example of model-assisted design strategies of a key-component for passive water treatment devices.

The results presented in this work show the interconnection between the different heat and mass transfer mechanisms involved in porous media. Depending on each specific application, some mechanisms might predominate over others: for instance, as demonstrated in section 3.2.2, drying of small, capillary-efficient components might be simulated without the related wicking transient, as it would be negligible with respect to the whole process even for small volumes of water; on the other hand, radiative heat transfer is fundamental when solar irradiance is involved, especially for external conditions in the range  $RH > 0.4$  and  $T_a < 30^\circ\text{C}$ . As a consequence, the most relevant transfer mechanisms to be simulated and the target functionality to be maximised are extremely application-dependent and,

thus, should be identified on a case by case approach. Nevertheless, the comprehensive heat and mass transfer model discussed in this work plays a crucial role in determining the key physical properties and geometrical features of passive and energy-efficient devices with optimised wicking and evaporation performance.

## Acknowledgements

This work was supported by the MIT International Science and Technology Initiatives (MIT - Italy MITOR Project n. 2018).

## Competing interests

The authors declare no competing interests.

## References

- [1] R. Masoodi, K. M. Pillai, Wicking in porous materials: traditional and modern modeling approaches, CRC Press, 2012.
- [2] G. Righetti, L. Doretto, H. Sadafi, K. Hooman, S. Mancin, Water pool boiling across low pore density aluminum foams, *Heat Transfer Engineering* 41 (19-20) (2020) 1673–1682.
- [3] M. M. Nahar, B. Ma, K. Guye, Q. H. Chau, J. Padilla, M. Iyengar, D. Agonafer, Microscale evaporative cooling technologies for high heat flux microelectronics devices: Background and recent advances, *Applied Thermal Engineering* (2021) 117109.
- [4] M. Alberghini, S. Hong, L. M. Lozano, V. Korolovych, Y. Huang, F. Signorato, S. H. Zandavi, C. Fucetola, I. Ulu-turk, M. Y. Tolstorukov, et al., Sustainable polyethylene fabrics with engineered moisture transport for passive cooling, *Nature Sustainability* (2021) 1–10.
- [5] P.-C. Hsu, A. Y. Song, P. B. Catrysse, C. Liu, Y. Peng, J. Xie, S. Fan, Y. Cui, Radiative human body cooling by nanoporous polyethylene textile, *Science* 353 (6303) (2016) 1019–1023.
- [6] B. Dai, K. Li, L. Shi, X. Wan, X. Liu, F. Zhang, L. Jiang, S. Wang, Bioinspired janus textile with conical micropores for human body moisture and thermal management, *Advanced Materials* 31 (41) (2019) 1904113.
- [7] V. Kashyap, H. Ghasemi, Solar heat localization: concept and emerging applications, *Journal of Materials Chemistry A* 8 (15) (2020) 7035–7065.
- [8] M. Morciano, M. Fasano, S. V. Boriskina, E. Chiavazzo, P. Asinari, Solar passive distiller with high productivity and marangoni effect-driven salt rejection, *Energy & Environmental Science* 13 (10) (2020) 3646–3655.
- [9] E. Chiavazzo, M. Morciano, F. Viglino, M. Fasano, P. Asinari, Passive solar high-yield seawater desalination by modular and low-cost distillation, *Nature Sustainability* 1 (12) (2018) 763–772.
- [10] M. Morciano, M. Fasano, L. Bergamasco, A. Albiero, M. L. Curzio, P. Asinari, E. Chiavazzo, Sustainable freshwater production using passive membrane distillation and waste heat recovery from portable generator sets, *Applied Energy* 258 (2020) 114086.
- [11] S. W. Sharshir, M. Elkadeem, A. Meng, Performance enhancement of pyramid solar distiller using nanofluid integrated with v-corrugated absorber and wick: An experimental study, *Applied Thermal Engineering* 168 (2020) 114848.
- [12] X. Li, G. Xu, G. Peng, N. Yang, W. Yu, C. Deng, Efficiency enhancement on the solar steam generation by wick materials with wrapped graphene nanoparticles, *Applied Thermal Engineering* 161 (2019) 114195.

- [13] L. Mascaretti, A. Schirato, R. Zbořil, Š. Kment, P. Schmuki, A. Alabastri, A. Naldoni, Solar steam generation on scalable ultrathin thermoplasmonic tin nanocavity arrays, *Nano Energy* 83 (2021) 105828.
- [14] Y. Chen, Y. Zheng, Bioinspired micro-/nanostructure fibers with a water collecting property, *Nanoscale* 6 (14) (2014) 7703–7714.
- [15] Y. Gao, J. Wang, W. Xia, X. Mou, Z. Cai, Reusable hydrophilic–superhydrophobic patterned weft backed woven fabric for high-efficiency water-harvesting application, *ACS Sustainable Chemistry & Engineering* 6 (6) (2018) 7216–7220.
- [16] M. Rana, J.-T. Chen, S. Yang, P.-C. Ma, Biomimetic superoleophobicity of cotton fabrics for efficient oil–water separation, *Advanced Materials Interfaces* 3 (16) (2016) 1600128.
- [17] M. Alberghini, M. Morciano, M. Fasano, F. Bertiglia, V. Fericola, P. Asinari, E. Chiavazzo, Multistage and passive cooling process driven by salinity difference, *Science advances* 6 (11) (2020) eaax5015.
- [18] P. Xu, X. Ma, X. Zhao, K. S. Fancey, Experimental investigation on performance of fabrics for indirect evaporative cooling applications, *Building and Environment* 110 (2016) 104–114.
- [19] M. Auliano, D. Auliano, M. Fernandez, P. Asinari, C. A. Dorao, Can wicking control droplet cooling?, *Langmuir* 35 (20) (2019) 6562–6570.
- [20] A. V. Bazilevsky, A. L. Yarin, C. M. Megaridis, Co-electrospinning of core-shell fibers using a single-nozzle technique, *Langmuir* 23 (5) (2007) 2311–2314.
- [21] S. Shen, A. Henry, J. Tong, R. Zheng, G. Chen, Polyethylene nanofibers with very high thermal conductivities, *Nature nanotechnology* 5 (4) (2010) 251–255.
- [22] J. Van Dingenen, High performance dyneema fibres in composites, *Materials & Design* 10 (2) (1989) 101–104.
- [23] C. Balocco, L. Mercatelli, N. Azzali, M. Meucci, G. Grazzini, Experimental transmittance of polyethylene films in the solar and infrared wavelengths, *Solar Energy* 165 (2018) 199–205.
- [24] S. V. Boriskina, An ode to polyethylene, *MRS Energy & Sustainability* 6 (2019).
- [25] Higgs Materials Sustainability Index, <https://msi.higg.org/>, [Online; accessed 10-November-2020].
- [26] M. E. Grigore, Methods of recycling, properties and applications of recycled thermoplastic polymers, *Recycling* 2 (4) (2017) 24.
- [27] J. Dees, J. Spruiell, Structure development during melt spinning of linear polyethylene fibers, *Journal of Applied Polymer Science* 18 (4) (1974) 1053–1078.
- [28] G. Vaartstra, L. Zhang, Z. Lu, C. D. Díaz-Marín, J. C. Grossman, E. N. Wang, Capillary-fed, thin film evaporation devices, *Journal of Applied Physics* 128 (13) (2020) 130901.
- [29] N. Fries, K. Odic, M. Conrath, M. Dreyer, The effect of evaporation on the wicking of liquids into a metallic weave, *Journal of colloid and interface science* 321 (1) (2008) 118–129.
- [30] A. Perwuelz, P. Mondon, C. Caze, Experimental study of capillary flow in yarns, *Textile Research Journal* 70 (4) (2000) 333–339.
- [31] Y. Xia, Q. Hou, H. Jubaer, Y. Li, Y. Kang, S. Yuan, H. Liu, M. Wu, L. Zhang, L. Gao, et al., Spatially isolating salt crystallisation from water evaporation for continuous solar steam generation and salt harvesting, *Energy & Environmental Science* 12 (6) (2019) 1840–1847.
- [32] N. Xu, X. Hu, W. Xu, X. Li, L. Zhou, S. Zhu, J. Zhu, Mushrooms as efficient solar steam-generation devices, *Advanced Materials* 29 (28) (2017) 1606762.
- [33] Y. Shi, R. Li, Y. Jin, S. Zhuo, L. Shi, J. Chang, S. Hong, K.-C. Ng, P. Wang, A 3d photothermal structure toward improved energy efficiency in solar steam generation, *Joule* 2 (6) (2018) 1171–1186.
- [34] F. Signorato, M. Morciano, L. Bergamasco, M. Fasano, P. Asinari, Exergy analysis of solar desalination systems based on passive multi-effect membrane distillation, *Energy Reports* 6 (2020) 445–454.
- [35] X. Cheng, G. Yang, J. Wu, Recent advances in the optimization of evaporator wicks of vapor chambers: from mechanism to fabrication technologies, *Applied Thermal Engineering* (2021) 116611.
- [36] JCGM, Evaluation of measurement data—guide to the expression of uncertainty in measurement, Int. Organ. Stand. Geneva ISBN 50 (2008) 134.
- [37] H. Princen, Capillary phenomena in assemblies of parallel cylinders: I. capillary rise between two cylinders, *Journal of Colloid and Interface Science* 30 (1) (1969) 69–75.
- [38] H. Princen, Capillary phenomena in assemblies of parallel cylinders: II. capillary rise in systems with more than two cylinders, *Journal of Colloid and Interface Science* 30 (3) (1969) 359–371.
- [39] M. B. Allen III, Numerical modelling of multiphase flow in porous media, *Advances in Water Resources* 8 (4) (1985) 162–187.
- [40] Y. Mualem, A new model for predicting the hydraulic conductivity of unsaturated porous media, *Water resources research* 12 (3) (1976) 513–522.
- [41] J. Chen, J. Hopmans, M. Grismer, Parameter estimation of two-fluid capillary pressure-saturation and permeability functions, *Advances in Water Resources* 22 (5) (1999) 479–493.
- [42] M. T. Van Genuchten, A closed-form equation for predicting the hydraulic conductivity of unsaturated soils, *Soil science society of America journal* 44 (5) (1980) 892–898.
- [43] M. Nordlund, V. Michaud, Dynamic saturation curve measurement for resin flow in glass fibre reinforcement, *Composites Part A: Applied Science and Manufacturing* 43 (3) (2012) 333–343.
- [44] COMSOL Multiphysics, Two-phase flow in column, [https://www.comsol.it/model/download/667241/models.ssf.twophase\\_flow\\_column.pdf](https://www.comsol.it/model/download/667241/models.ssf.twophase_flow_column.pdf), [Online; accessed 04-November-2020].
- [45] F. E. Jones, Evaporation of water with emphasis on applications and measurements, CRC Press, 1991.
- [46] J. Fan, X. Cheng, X. Wen, W. Sun, An improved model of heat and moisture transfer with phase change and mobile condensates in fibrous insulation and comparison with experimental results, *International Journal of Heat and Mass Transfer* 47 (10–11) (2004) 2343–2352.
- [47] A. H. Persad, C. A. Ward, Expressions for the evaporation and condensation coefficients in the hertz-knudsen relation, *Chemical reviews* 116 (14) (2016) 7727–7767.
- [48] J. A. Duffie, W. A. Beckman, N. Blair, Solar engineering of thermal processes, photovoltaics and wind, John Wiley & Sons, 2020.
- [49] M. Alberghini, M. Morciano, L. Bergamasco, M. Fasano, L. Lavagna, G. Humbert, E. Sani, M. Pavese, E. Chiavazzo, P. Asinari, Coffee-based colloids for direct solar absorption, *Scientific reports* 9 (1) (2019) 1–11.
- [50] G. Ni, S. H. Zandavi, S. M. Javid, S. V. Boriskina, T. A. Cooper, G. Chen, A salt-rejecting floating solar still for low-cost desalination, *Energy & Environmental Science* 11 (6) (2018) 1510–1519.
- [51] B. N. Taylor, C. E. Kuyatt, Guidelines for evaluating and expressing the uncertainty of nist measurement results (1994).
- [52] H. Jasak, A. Jemcov, Z. Tukovic, et al., Openfoam: A c++ library for complex physics simulations, in: International workshop on coupled methods in numerical dynamics, Vol. 1000, IUC Dubrovnik Croatia, 2007, pp. 1–20.
- [53] A. Bejan, Convection heat transfer, John Wiley & sons, 2013.
- [54] M. Karaki, A. Hallal, R. Younes, F. Trochu, P. Lafon, A. Hayek, A. Kobeissy, A. Fayad, A comparative analytical, numerical and experimental analysis of the microscopic permeability of fiber bundles in composite materials, *Int. J. Compos. Mater* 7 (3) (2017) 82–102.